理學碩士 學位論文

Synthesis and TADF properties of boron emitters comprising rigid donor and acceptor units linked by a carbon–carbon bond triarylborane compounds

(견고한 주개와 받개를 탄소-탄소 결합을 한 붕소화합물의 합성과 TADF 특성)

蔚 山 大 學 校 大 學 院

化 學 科

辛 基 訓

Synthesis and TADF properties of boron emitters comprising rigid donor and acceptor units linked by a carbon–carbon bond triarylborane compounds

(견고한 주개와 받개를 탄소-탄소 결합을 한 붕소화합물의 합성과 TADF 특성)

指 導 敎 授 이 민 형

이 論文을 理學碩士 學位 論文으로 제출함

2021年 11月

蔚 山 大 學 校 大 學 院
化 學 科
李 炯 東

辛基訓의 理學碩士 學位 論文을 認准함.

審査委員　홍 종 욱 

審査委員　이 민 형 

審査委員　우 상 국 

蔚 山 大 學 校 大 學 院

2021년 11月

Synthesis and TADF properties of boron emitters comprising rigid donor and acceptor units linked by a carbon–carbon bond triarylborane compounds

Abstract

We report three rigid donor (D)-acceptor (A)-type thermally activated delayed fluorescence (TADF) compounds, CzMeBCO (**1**), BuCzMeBCO (**2**), and EtCzMeBCO (**3**), in which 9-substituted 9*H*-carbazole (9-RCz) donors are linked with a boron-carbonyl (BCO) hybrid acceptor by a carbon–carbon bond. In toluene solution, all compounds exhibit normal fluorescence in deep blue region (426–429 nm) with high photoluminescence quantum yields (PLQYs) of 77%–94% whereas they exhibit greenish blue to green emissions in PMMA film with distinct delayed fluorescence components. High PLQYs are also retained in their rigid state, showing 60%–85% in PMMA film. However, the PLQY and delayed fluorescence lifetime decrease with the increase of the doping concentration of compounds in the film state. The details of synthesis and photophysical properties of compounds will be discussed with theoretical study. Using the TADF emitters, normal performance TADF-OLEDs with maximum external quantum efficiencies of 14.7% for the skyblue (CzMeBCO) and 14.5% for the skyblue (BuCzMeBCO) are presented.

국문초록

우리는 9-치환된 9H-카바졸(9-RCz) 도너는 탄소-탄소 결합에 의해 붕소-카르보닐하이브리드 (BCO) 어셉터와 연결됩니다. 톨루엔 용액에서 모든 화합물은 77-94%의 높은 광발광 양자 수율(PLQY)로, 진한 파란색 영역(426-429 nm)에서 정상적인 형광을 나타내는 반면, 뚜렷한 지연 형광 특성이 있는 PMMA 필름에서는 청록색과 녹색을 방출합니다. 높은 PLQY도 단단한 상태로 유지 되어있는 PMMA 필름에서 60%-85%를 나타냅니다. 그러나 PLQY와 지연 형광 수명은 필름 상태에서 화합물의 도핑 농도가 증가함에 따라 감소합니다. 화합물의 합성 및 광물리학적 특성에 대한 자세한 내용은 이론적 연구와 함께 논의됩니다. TADF 발광체를 사용하여 하늘색인 CzMeBCO의 경우 최대 외부 양자 효율이 14.7%이고 하늘색인 BuCzMeBCO의 경우 14.5%인 일반적인 TADF-OLED성능을 보였습니다.

Contents

List of Figures

List of Schemes

List of Tables

I. Introduction

1. Organic light-emitting diodes (OLEDs)

Before OLED was commercialized, the first generation LCD and the second generation LED were mainly applied and used in displays. However, now, beyond the 1st and 2nd generations, OLED, which compensates for their shortcomings, is attracting attention as the 3rd generation display and research is underway. LED is a photoelectric conversion type semiconductor light emitting diode that converts electrical energy into light energy. This is a semiconductor device that emits light by recombination of minority carriers injected using the pn junction structure of the semiconductor two-terminal device However, organic light emitting diodes (OLEDs) display that emit light by a thin organic layer that forms a p-n junction.[1] The OLED light emission principle is that holes and electrons injected from the anode and cathode combine in the light emitting layer to emit light. Therefore, OLEDs do not need the backlight which is used to LCD and LED displays and resulted that OLED display can be thin and light. Moreover, OLEDs are better than LCD and LED that reason by low driving voltage, high brightness, full-color emission, rapid response, easy fabrication of potentially large area and flexible thin-film devices. It's especially better in the color reproducibility and darkness ratio. In the early 1950s, first OLED concept was discovered by André Bernanose and co-workers at the Nancy-Université in France. This was the first to observe organic material electroluminescence by depositing organic materials on thin films of cellulose or cellophane or by dissolving them in materials such as acridine orange and applying high alternating voltages in air.[2,19] In 1960, ohmic dark implanted electrode contacts to organic crystals were developed by Martin Pope and his co-workers at New York University, which described the energetic requirements for hole and electron injection electrode contact, which became the basis for charge injection in all modern OLED devices. Since the first discovery of luminescence in anthracene single crystal by W.Helfirich, *et al*. in 1965, Tang and VanSlyke at Eastman Kodak reported the double-layered device using tris(8-hydroxyquinoline) aluminum (Alq_3) as the emitting and electron-transporting layer in 1987.[3,4] They reported that tris(8-hydroxyquinoline) aluminum (Alq_3) lowered the device's driving voltage to less than 10V and improved the efficiency to 1.5lm/W.

Electroluminescence (EL) performance is improved 2-3 times using the doping method.[4] Through their research report, many research groups were actively involved in the study of electroluminescence. Commercialization began in 1997 when flat displays that used the form of organic polymers light emitting OLEDs were applied to automotive stereo displays. Nowadays, various products are being produced based on the advantages of OLED. In particular, more and more products are applied with thinner displays to emit light on their own, and wearable displays are being developed a lot using flexible features. In addition, by increasing the production yield and upgrading the vacuum deposition technology, the price is getting cheaper and the demand is increasing, and LED and LCD are being replaced by OLED. However, among the three primary colors of light, red and green, the drawbacks of OLED, such as short lifetime and sharp drop-off with higher efficiency, have been resolved to some extent as the 2nd generation OLED shifts, but the blue OLED is still in the 1st generation and has low efficiency. It remains a task to be done. Therefore, the cause of the above problems must be solved through various methods such as spin effect, designing various compounds, and light extraction.

1-2. Multi-layer OLEDs

Since OLED is a charge injection type light emitting device, the charge injection efficiency between each interface is the factor that has the greatest influence on the device performance. The general structure of OLED is to form transparent ITO (indium tin oxide) which is typically compose as an oxygen-saturated composition with a formulation of 74% In, 18% O2, and 8% Sn by weight. It has the characteristics that the anode and cathode selected according to electrical conductivity and chemical stability are well transmitted on a transparent substrate with good light permeability,[5,6] and on top of that, several products with different transport capabilities are formed. It has a structure in which a multilayer thin film of organic material and a cathode of an Mg-Ag alloy are sequentially formed. It is a structure in which cathodes are sequentially formed. The multilayer thin film consists of hole injection layer (HIL), hole transport layer(HTL), emitting layer (EML: Emitting Layer), Al-Poly (p- It is composed of an electron transport layer (ETL), electron injection layer (EIL) and this

organic thin film is about 100 nm. The main purposes of this general structure are reducing each injection barrier promotes charge carrier injection. Also, the recombination region is moved to the center of the device, preventing quenching of excitons in the electrode.[7] A hole injection layer (HIL) is contained a metal complex salt of Co or Ga or PEDOT:PSS or Cu-PC and that is located between the anode and the hole transport layer to lower the hole injection energy barrier.[8] In the hole transport layer(HTL), electron-donating molecules with a small ionization potential are used to facilitate hole injection from the anode, and styrene, benzoxazine, benzocyclobutane, diamine, triamine, and tetraamine derivatives based on triphenylamine are mainly used.[9] An emitting layer (EML: Emitting Layer) is a layer that emits red, blue, and green light by recombination of injected electrons and holes, and the spectrum is determined according to the binding energy in the light emitting layer. Therefore, the luminous color is determined depending on the luminescent layer forming material. This layer can be a material made of organic molecules or polymers with high efficiency, lifetime and color purity.[8] Al-Poly which is composed of an electron transport layer (ETL) such as phenylene vinylene mainly uses Bebq2 PBD, OXD, TAZ, etc. to smoothly transport the electrons supplied from the cathode to the light emitting layer and suppress the movement of unbound holes in the light emitting layer to increase the chance of recombination in the light emitting layer.[8] In particular, some devices use an electron injection layer because OLED is a current-driven device through which a large amount of current flows, and this potential drop causes energy and efficiency losses. Additionally, the large potential drop across these layers causes Joule heating, leading to device failure. Therefore, efficient organic material-based devices require a reduction in the barriers faced by charge carriers while traversing the path from each electrode to the active layer of the device. The choice of these charge injection and transport layers is also an important issue. To this end, there have been several attempts to use an electron injection buffer layer or a low work function cathode to easily inject electrons from the cathode.[10] Electron affinity, cathode It should have excellent adhesion to the electrode. The cathode is usually a low work function metal alloy ($\varphi w \approx 2.9–4.0$ eV). The cathode injects electrons into the emissive layer. It should be transparent in the top emission device and stable to the organic layer below it.[8] In conventional OLEDs, the charge carriers (holes and electrons) are unbalanced. So, When holes pass through the light emitting layer and go to the cathode, the lifetime and efficiency of the device are reduced. In some cases,

the insertion of a hole blocking layer (HBL) with a very low HOMO level in an OLED which is formed on the light emitting layer helps to modify the charge carrier balance, improve brightness and emission efficiency, or confine excitons within the emissive layer.[11] Contrary to the method of preventing the cathode from reaching the anode, material properties of the hole transport layer and the hole injection layer with a high LUMO level are sometimes required to prevent electrons from reaching the anode.

Table. 1 [8]

Materials generally used in different layers of OLED's.

Layer of OLED's	Materials generally used in different layers of OLED's
Anode	High work function; ITO, IZO, ZNO; TCP (PANI, PEDOT); Au, Pt, Ni, p-Si; ITO; Surface treatment; Plasma (O_2, NH_3); Solution (Aquaregia); Thin insulator AlO_x, SiO_x; RuO_x (4.9 eV); MoO_x (5.4 eV)
Cathode	Low work function; Mg:Ag; Li:Al; Ca. . .; thin insulator; LiF; MgO_x.
HIL	HOMO level; Spiro-TAD; CuPc; m-MTDATA; PTCDA; 2TNATA; TPD; NPD; DPVBi, . . .; PPV; PVK; Dendrimer
ETL	LUMO level; Alq_3; $Bebq_2$; PBD; OXD; TAZ; BCP
EML: Dopant	Alq_3; CPB; Balq; DPVBi; Rubrene; Spiro DPVBi; Quinacridone; Coumarin; DSA; $Ir(ppy)_3$; Pt(OEP); emitting assistant; rare earth complexes

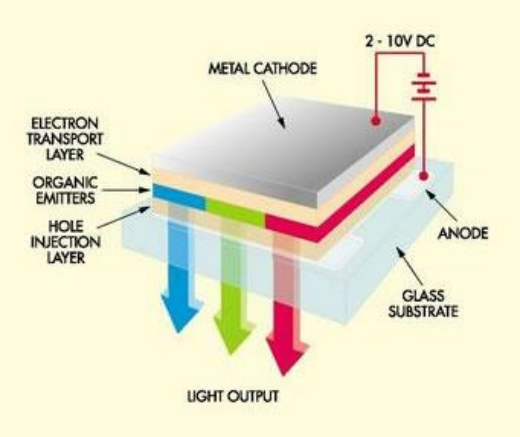

Figure 1. Schematic overview of OLED device.

1-3. Working Principle of OLEDs

A current flows from cathode to anode through the device as electrons are injected from the cathode into the LUMO of the organic layer and exit from the HOMO at the anode. Electrostatic forces attract electrons and holes to each other and combine to form excitons. Since electrons and holes are fermions with a spin S=1/2, when they meet and recombine to

form an exciton in a certain part of the luminous body, the triplet exciton with S=1 and the two spins are symmetrically arranged. Singlet excitons with S=0 arranged antisymmetrically are generated in a ratio of 3:1.[12] The decay from the triplet state increases the time since the spin is before inhibition and adversely affects the internal efficiency of the fluorescent device. In contrast, phosphorescent organic light emitting diodes use spin-orbit interactions to promote intersystem crossing (ISC) between singlet and triplet states, thereby increasing internal efficiency in such a way that electrons move from singlet to triplet states and emit.[13,14] Light is generated as these excitons move to the ground state. At this time, the wavelength length representing the color is determined by the energy difference between HOMO and LUMO, and the generated light is emitted toward the anode, which is a transparent electrode.

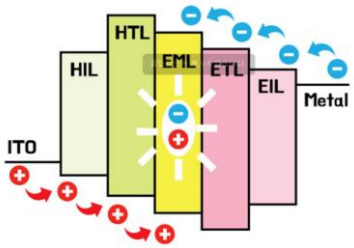

Figure 2. Working principle of OLEDs

1-4. Thermally Activated Delayed Fluorescence (TADF)

So far, the types of OLED are divided into three generations. The first generation is fluorescence, which is emitted only in the singlet state, so the efficiency is very low with 25% internal quantum efficiency (IQE), but the color purity is very good. The second generation typically uses heavy metals as phosphorescence. The second generation typically uses heavy metals as phosphorescence, 75% triplet excitons in triplet state are used. 25% singlet excitons in singlet state also are used through intersystem crossing (ISC) with spin orbit coupling (SOC) due to heavy metal properties. As a result, 100% IQE can be achieved, and color purity is good, just like the first generation.[15] However, using heavy metals such as Ir and Pt, it is expensive, unstable, and has a very long lifetime.[13] The 3rd generation TADF uses singlet and triplet excitons as in phosphorescence. Contrary to phosphorescence, excitons reversing intersystem crossing (RISC) from triplet state to singlet state can give 100% IQE.[16] (**Figure.**

3) It is made of purely organic material and has the advantage of low cost and short lifetime, but has the disadvantage of low color purity.

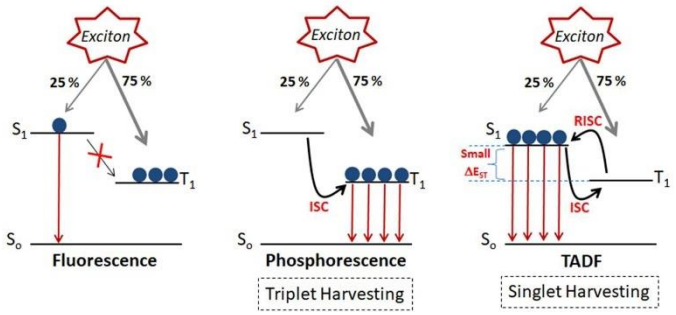

Figure 3. The Generation of OLEDs.

The most important value during the TADF process is the ΔE_{ST} value, which is the interval between the singlet excited state and the triplet excited state. The optimal condition for this is $\Delta E_{ST} < 0.2$ eV. Also, there must be a twist between donor and acceptor. The reason is that there have a dihedral angles through twist between the donor and the acceptor, So the HOMO and LUMO have well be separated and then the overlap rate of conjugation is reduced, thereby reducing ΔE_{ST}, increasing the SOC, and can have fast RISC and strong molecular CT excited states.[17,18,19] Having strong SOC and RISC can reduce phenomena such as triplet−triplet annihilation (TTA), sin-glet−triplet annihilation (STA), and exciton−polaron quenching, thereby improving roll-off.[20]

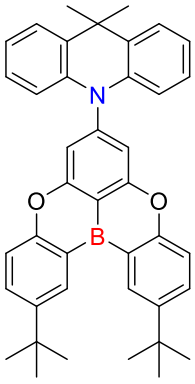

TDBA–Ac

Nat. Photonics, 2019, 13, 540-546

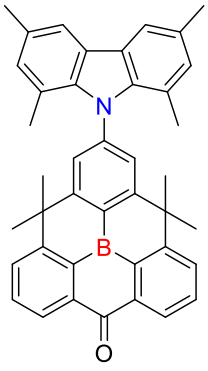

TMCzBCO

CEJ, 2021, 423, 130224

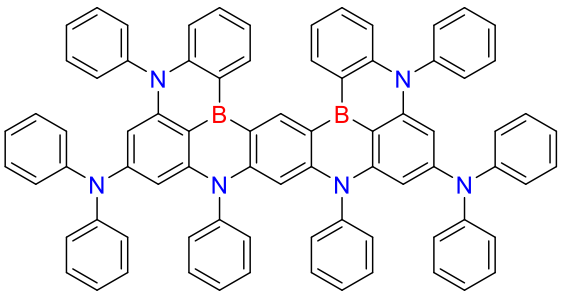

υ–DABNA

Nat. Photonics, 2019,13, 678-682

Figure 4. Structures of TADF emitters for OLEDs**.**

Therefore molecular rigidity is important to achieve TADF efficiently. Different conformations of a molecule can yield different TADF efficiencies, consequently flexible donors or acceptors should be avoided.[15],[17]

2. TADF emitters containing triarylboron

Among the many reports on OLED, there are many acceptors containing boron. It has come a long way since the concept of triaylborane was first published by Willams and Kaim.[20,21,22] The reason is that it does not satisfy the boron octect rule, so it can act as an excellent acceptor through p-π* conjugation between the empty p orbital at the center of boron and the π-conjugation framework of the aryl group bonded to boron. the boron center can be protected from attack by nucleophilic substances such as water in the air by substituting a bulky aromatic group because it is easily attacked by nucleophiles due to the nature of boron, which is an electrophile.[13] In addition, sufficient kinetic stability and large three-dimensional volume can be formed **(Figure. 5).** Yamaguchi and coworkers synthesized triphenylborane and 9,10-diphenyl-9,10-dihydro-9,10-diboraanthracene with additional structural constraints based on this system, and reported for the first time proving the kinetic stability of triphenylborane **(Figure 6)**.[23] In a form surrounding the aromatic group around boron, the structure is solid and locked through the connection between aromatic groups, so it is kinetically stable from nucleophilic attack by Lewis basis. When the above properties of triarylborane are applied to TADF, triarylboran which is strong Lewis acid acts as a good acceptor for the D-A organic π-conjugated system, and can emit strong intramolecular charge-transfer (ICT) by combining with a donor which has a large electronic dipole.[24]

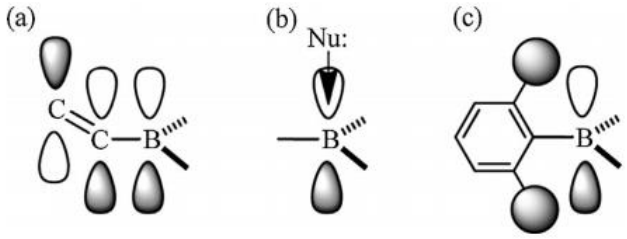

Figure 5. Characteristic features of boron atom in the tryarylborane π-conjugated system.

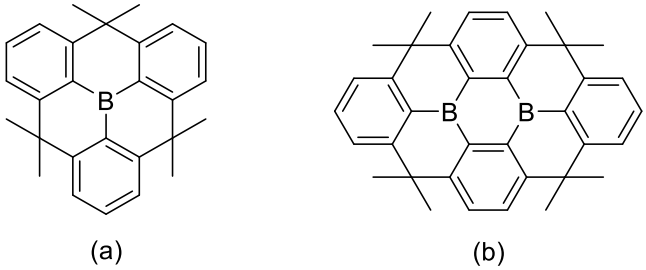

Figure 6. (a) triphenylborane, (b) 9,10-diphenyl-9,10-dihydro-9,10-diboraanthracene

3. Research Scopes

While many TADF-related compounds have been reported, it is still challenging as device lifetime and stability have not been resolved . To solve this, it is necessary to improve the SOC to reduce triplet-triplet annihilation (TTA), sin-glet-triplet annihilation (STA), and exciton-polaron quenching, which typically increase exciton deactivation processes and to strengthen the bond between donor and acceptor. Recently, it has been reported that the triaylborane type BCO acceptor dramatically reduces the lifetime through fast RISC caused by n-π*[20]. The strong electron-accepting of triaylborane was further improved by bonding a carbonyl group to triaylborane. Furthermore, the CT excited state characteristic of the parent triarylboron dominant π(Ar) to pz(B) could be deactivated, which is not suitable for achieving effective SOC with the 1CT state of the emitter.[20] while SOC and RISC usually occur between 1CT(S1) and 3CT(T1), In the case of the BCO acceptor, n-π* state of the carbonyl group is located in 3LE (T2) and a 3nπ* state could provide a viable route to allow the effective SOC with the 1CT state. so strong SOC and fast RISC occurred in 1CT-3LE, which is shorter than ΔEST of 1CT-3CT. Therefore, we targeted a compound with higher device efficiency by strengthening the bond between the BCO acceptor and donor with these properties. So, we targeted a compound with higher device efficiency by strengthening the bond between the BCO acceptor and donor with these properties. Herein, we report three planar donor-acceptor type TADF emitters, CzMeBCO(**1**), BuCzMeBCO(**2**) and EtCzMeBCO(**3**). Stronger bonding and stability were expected by connecting the donor of the planar carbazole structure and the acceptor with a C-C bond through the Suzuki reaction. In solution, all compounds exhibit normal

fluorescence in deep blue region (426-429 nm) with the PLQY of 93% for (**2**) , 79% for (1) and 77% for (3). However, in the film doped with PMMA, all compounds exhibit the color(skyblue, green) and delay lifetime (1-16 μs) with the PLQY of 85% for (**2**) , 78% for (1) and 60% for (3). Through TGA, it was confirmed that (2) with Td_5 of 405 °C had good thermal stability.

II. Experiment

1. Chemical and instrumentation

All operations were performed under an inert nitrogen atmosphere using standard Schlenk and glovebox techniques. Anhydrous grade solvents (Aldrich) were dried by passing them through an activated alumina column and stored over activated molecular sieves (5 Å). Spectrophotometric-grade solvents for photophysical measurements were used as received from Aldrich and Merck. Commercial reagents were used without further purification after purchase. Deuterated solvents from Cambridge isotope Laboratories were used. NMR spectra were recorded on a Bruker AM 300 (300.13 MHz for ^{1}H, 75.48 MHz for ^{13}C, 96.29 MHz for ^{11}B) spectrometer at ambient temperature. Chemical shifts are given in parts per million (ppm), and are referenced against external Me_4Si (^{1}H, ^{13}C), BF_3OEt_2 (δ 0 ppm, ^{11}B). Elemental analyses were performed on a Flash 2000 elemental analyzer (Thermo Scientific) at University of Ulsan. Melting point (mp) was measured by Melting Point Apparatus SMP30 (Stuart Equipment). Thermogravimetric analysis (TGA) was performed with a TA Instruments Q50 under an N_2 atmosphere at a heating rate of 10 °C/min. Mass spectra were obtained on a JEOL JMS700 high-resolution FAB-mass spectrometer (HR FAB-MS) at the Korea Basic Science Institute, Daegu, Korea. Cyclic voltammetry experiments were performed using an Autolab/PGSTAT101 system.

2. Synthesis

All compounds were prepared according to **Scheme 1.** 2-bromo-4,4,12,12-tetramethyl-4,12-dihydro-8*H*-3a2-boradibenzo[cd,mn]pyren-8-one (Br-BCO) were prepared from the reported procedure.[13] Full experimental details are given below.

4,4'-Dimethyl-2-nitro-1,1'-biphenyl (1a)

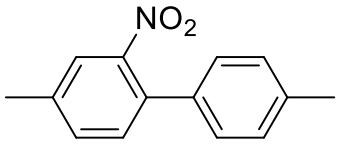

A suspension of 4,4'-dimethyl-1,1'-biphenyl (1.0 g, 5.49 mmol) in Acetic acid(20 mL, 347 mmol) was stirred and heated to 80 °C for 30 min under air atmosphere. The reaction mixture was cooled to room temperature, and nitric acid(8 mL, 40.0 mmol) was added dropwise. After the reaction mixture was heated for 1 h, the distilled ice water (100 mL) was added. The organic layer was separated and the aqueous layer was extracted with dichloromethane (100 mL) three times. The combined organic layer was dried over MgSO4, filtered, and evaporated under reduced pressure. The crude product was purified by column chromatography using CH_2Cl_2/*n*-hexane (1:3, v/v) as an eluent to give **1a** as a yellow powder (Yield: 1.09 g, 87%). ^{1}H NMR ($CDCl_3$) δ 7.63 (d, J = 0.7 Hz, 1H), 7.41–7.38 (m, 1H), 7.31 (d, J = 7.8 Hz, 1H), 7.24–7.17 (m, 4H), 2.46 (s, 3H), 2.39 (s, 3H).

2,7-Dimethyl-9*H*-carbazole (2a)

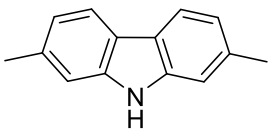

To a solution of (1) (1.086 g, 4.78 mmol) and triphenylphosphine (3.13 g, 11.9 mmol) were placed and dissolved in 1,2-dichlorobenzene (6.5 mL). The reaction mixture was refluxed for 16 h. After the mixture was cooled to room temperature, and removed a solution under reduced pressure and condenses at 70 °C. a diethyl ether solution (100 mL) was added carefully and stirred for 1h. After the filter cake was washed with diethyl ether, and evaporated under reduced pressure. The obtained crude product was purified by silica gel column chromatography (diethyl ether/hexane = 1/2, v/v) and recrystallized to give 0.508 g (48.7 mmol) of **2a** in 54% yield as white solids.1H NMR ($CDCl_3$) δ 7.90 (d, J = 7.9 Hz, 1H), 7.17 (sq, 1H), 7.04 (dd, J = 7.8, 0.8 Hz, 1H), 2.52 (s, 3H).

3-Bromo-2,7-dimethyl-9*H*-carbazole (3a)

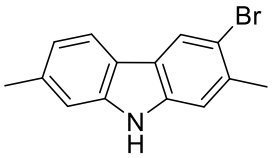

To a solution of NBS (3.13 g, 11.9 mmol) in dry DMC (200 mL) cooled at -78°C was added dropwise (1) (1.086 g, 4.78 mmol) in dry DMC (200 mL) under nitrogen for 0.5 h. After worming up to room temperature, distilled water (100 mL) was slowly added and a turbid mixture was extracted with CH_2Cl_2 (50 mL × 3). The organic layer was dried over $MgSO_4$, filtered, and concentrated under reduced pressure. The crude product was purified by silica gel column chromatography using CH_2Cl_2/*n*-hexane (1:5, v/v) as an eluent to give **3a** as a white powder (yield: 1.03 g, 57%). ^{1}H NMR (CD_2Cl_2) δ 8.16 (s, 1H), 7.85 (d, J = 8.0 Hz, 1H), 7.33 (s, 1H), 7.24 (sq, 1H), 7.051 (dq, J = 8.1, 0.9 Hz, 1H), 2.52 (d, J = 8.1 Hz, 6H).

(3-Bromo-2,7-dimethyl-9-phenyl-9*H*-carbazole) (1b)

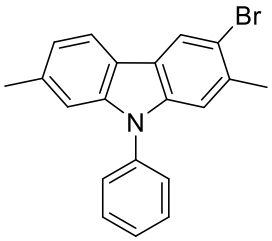

To a solution of **3a** (0.2 g, 0.73 mmol) and copper(I) iodide (0.07 g, 0.37 mmol) and potassium carbonate (0.3 g, 2.17 mmol) in dry DMF (10 mL) was added iodobenzene (0.4 mL, 3.63 mmol). After the completion of the addition, the mixture solution was refluxed for 16 h. After the mixture was cooled to room temperature, The resulting solution was quenched by the addition of a saturated aqueous NH_4Cl solution (100 mL), extract with ethyl acetate (30 mL × 3). The combined organic layer was dried over $MgSO_4$, filtered and concentrated under reduced pressure. The crude product was purified by silica gel column chromatography using CH_2Cl_2/*n*-hexane (1:5, v/v) as an eluent to give **1b** as a white powder (yield: 0.204 g, 80%). ^{1}H NMR (CD_2Cl_2) δ 8.23 (s, 1H), 7.92 (d, J = 7.8 Hz, 1H), 7.66–7.49 (m, 5H), 7.25 (s, 1H), 7.16 (s, 1H), 7.10 (dd, J = 8.1, 0.9 Hz, 1H), 2.47 (d, J = 7.5 Hz, 6H). ^{13}C NMR ($CDCl_3$) δ 141.64, 140.33, 137.51, 136.52, 135.48, 134.51, 130.06, 127.65, 127.20, 123.35, 123.19, 121.73, 120.06, 119.93, 115.71, 111.25, 110.47, 109.98, 23.91, 22.18. HRMS (EI): *m/z* $[M]^+$ calcd for $C_{20}H_{16}BrN$: 349.0466; found: 349.0464.

(3-Bromo-9-(4-(*tert*-butyl)phenyl)-2,7-dimethyl-9*H*-carbazole) (2b)

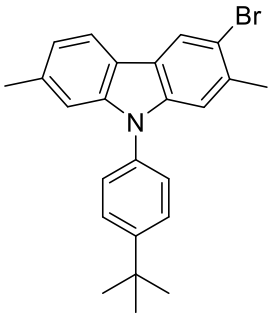

To a solution of **3a** (0.5 g, 1.82 mmol) and copper(I) iodide (0.17 g, 0.89 mmol) and potassium carbonate(0.76 g, 5.50 mol) in dry DMF (10 mL) was added 4-iodo-*tert*-butylbenzene (1.62 mL, 9.12 mmol). After the completion of the addition, the mixture solution was refluxed for 16 h. After the mixture was cooled to room temperature, The resulting solution was quenched by the addition of a saturated aqueous NH_4Cl solution (100 mL), extract with ethyl acetate (30 mL × 3). The combined organic layer was dried over $MgSO_4$, filtered and concentrated under reduced pressure. The crude product was purified by silica gel column chromatography using CH_2Cl_2/*n*-hexane (1:5, v/v) as an eluent to give **2b** as a white powder (yield: 0.51 g, 68%). ^{1}H NMR ($CDCl_3$) δ 8.22 (s, 1H), 7.92 (d, J = 7.8 Hz, 1H), 7.61 (dt, J = 8.7 Hz, 2H), 7.43 (dt, J = 8.7 Hz, 2H), 7.23 (s, 1H), 7.16 (s, 1H), 7.09 (d, J = 7.8 Hz, 1H), 2.49 (d, J = 6.6 Hz, 6H), 1.44 (s, 9H). ^{13}C NMR ($CDCl_3$) δ 150.60, 141.74, 140.44, 136.40, 134.70, 134.39, 126.84, 126.58, 123.27, 123.09, 121.56, 119.97, 119.86, 115.53, 111.36, 110.08, 34.84, 31.46, 23.86, 22.16. HRMS (EI): *m/z* $[M]^+$ calcd for $C_{24}H_{24}BrN$: 405.1092; found: 405.1092.

(3-Bromo-9-ethyl-2,7-dimethyl-9*H*-carbazole) (3b)

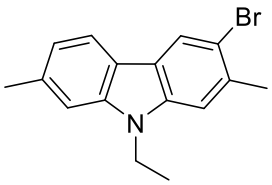

To a solution of **3a** (0.3 g, 1.09 mmol) and potassium hydroxide (0.38 g, 6.84 mmol) in dry DMF (10 mL) was allowed to stir at room temperature for 0.5 h. the reaction mixture was added iodoethane (0.13 mL, 1.64 mmol). After the completion of the addition, the mixture solution was stirred at room temperature for 16 h. The resulting solution was quenched by the addition of a distilled water (100 mL), precipitated white solids were collected via vacuum filtration to give **3b** as a white powder (yield: 0.3 g, 89%). ^{1}H NMR ($CDCl_3$) δ 8.18 (s, 1H), 7.88 (d, J = 7.9 Hz, 1H), 7.24 (s, 1H), 7.17 (s, 1H), 7.05 (d, J = 7.9 Hz, 1H), 4.28 (q, J = 7.2 Hz, 2H), 2.57 (d, J = 7.1 Hz, 6H), 1.41 (td, J = 7.3, 3.7 Hz, 3H). ^{13}C NMR ($CDCl_3$) δ 140.62, 139.33, 136.09, 134.01, 123.41, 122.79, 120.60, 120.02, 119.70, 114.58, 110.00, 108.79, 37.44,

24.06, 22.31, 13.75. HRMS (EI): *m/z* $[M]^+$ calcd for $C_{16}H_{16}BrN$: 301.0466; found: 301.0464.

2-(2,7-Dimethyl-9-phenyl-9*H*-carbazol-3-yl)-4,4,12,12-tetramethyl-4,12-dihydro-8*H*-3a2-boradibenzo[cd,mn]pyren-8-one (CzMeBCO, 1d)

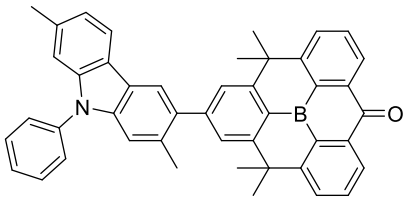

3-Bromo-2,7-dimethyl-9-phenyl-9*H*-carbazole (300 mg, 0.857 mmol) was treated with *n*-BuLi (0.33 mL, 0.824 mmol) in THF (20 mL) at -78 °C. After stirring for 1 h, $B(OMe)_3$ (0.29mL, 2.601 mmol) was added to the reaction mixture and further stirred for 1 h. The reaction mixture was acidified with 1.0 M HCl (50 mL) at 298 K. The crude product was separated and washed with n-hexane. The resulting (2,7-dimethyl-9-phenyl-9*H*-carbazol-3-yl)boronic acid (0.170 mg, 0.540 mmol), was combined with Br-BCO (210 mg, 0.492 mmol) in the presence of $Pd(PPh_3)_4$ (28 mg, 0.024 mmol) and K_2CO_3 (100 mg, 0.724 mmol) in THF/H_2O (3:1, v/v, 10 mL). The mixture was refluxed at 90 °C overnight. After cooling down to room temperature, the reaction mixture was filtered using celite pad and washed with dichloromethane. The filtrate was concentrated under reduced pressure and purified by column chromatography on silica gel using dichloromethane/*n*-hexane (1:3, v/v) as eluent to afford **CzMeBCO** as a bright yellow solid (Yield: 131 mg, 43%). ^{1}H NMR (CD_2Cl_2) δ 8.25 (dd, J = 7.8, 0.9 Hz, 2H), 8.09 (s, 1H), 8.10–8.00 (m, 3H), 7.82 (m, 4H), 7.72–7.60 (m, 4H), 7.53 (m, 1H), 7.36 (s, 1H), 7.24 (sq, 1H), 7.13 (dq, J = 8.1 Hz, 1H), 2.49 (d, J = 2.1 Hz, 6H), 1.87 (s, 12H). ^{13}C NMR (CD_2Cl_2) δ 188.99, 156.28, 156.16, 148.70, 141.72, 140.75, 138.21, 137.73, 136.23, 135.09, 133.43, 133.30, 131.46, 129.96, 127.47, 127.15, 126.20, 125.32, 121.67, 121.56, 121.06, 121.00, 119.77, 110.99, 109.96, 43.12, 33.25, 21.85, 21.50. ^{11}B NMR ($CDCl_3$): δ 47.8. Anal. calcd (%) for $C_{45}H_{36}BNO$: C 87.52, H 5.88, N 2.27; found: C 87.14, H 6.23, N 2.21.

2-(9-(4-(*tert*-Butyl)phenyl)-2,7-dimethyl-9*H*-carbazol-3-yl)-4,4,12,12-tetramethyl-4,12-dihydro-8*H*-3a2-boradibenzo[cd,mn]pyren-8-one (BuCzMeBCO, 2d)

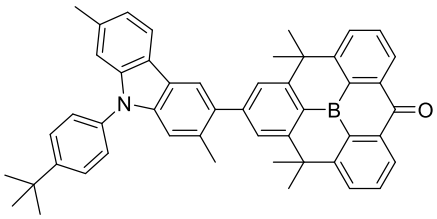

3-Bromo-9-(4-(*tert*-butyl)phenyl)-2,7-dimethyl-9*H*-carbazole (445 mg, 1.10 mmol) was treated with *n*-BuLi (0.43 mL, 1.04 mmol) in THF (20 mL) at -78 °C. After stirring for 1 h, $B(OMe)_3$ (0.37mL, 3.29 mmol) was added to the reaction mixture and further stirred for 1 h. The reaction mixture was acidified with 1.0 M HCl (50 mL) at 298 K. The crude product was separated and washed with n-hexane. The resulting (9-(4-(*tert*-butyl)phenyl)-2,7-dimethyl-9*H*-carbazol-3-yl)boronic acid (278 mg, 0.749 mmol), was combined with Br-BCO (288 mg, 0.674 mmol) in the presence of $Pd(PPh_3)_4$ (39 mg, 0.034 mmol) and K_2CO_3 (145 mg, 1.05 mmol) in THF/H_2O (3:1, v/v, 10 mL). The mixture was refluxed at 90 °C overnight. After cooling down to room temperature, the reaction mixture was filtered using celite pad and washed with dichloromethane. The filtrate was concentrated under reduced pressure and purified by column chromatography on silica gel using dichloromethane/*n*-hexane (1:3, v/v) as eluent to afford **BuMeBCO** as a bright yellow solid (Yield: 252 mg, 55%). Single crystals suitable for an X-ray diffraction study were obtained by vapor diffusion of methanol into a $C_2H_4Cl_2$ solution of **BuMeBCO**, affording colorless crystals. ^{1}H NMR (CD_2Cl_2) δ 8.26 (dd, J = 5.7, 0.6 Hz, 2H), 8.10 (s, 1H), 8.03 (dd, J = 11.4, 4.2 Hz, 3H), 7.85–7.82 (m, 4H), 7.69 (dt, J = 6.6 Hz, 2H), 7.57–7.53 (m, 2H), 7.37 (s, 1H), 7.25 (s, 1H), 7.12 (dd, J = 6.0, 0.6 Hz, 1H), 2.50 (d, J = 1.2 Hz, 6H), 1.86 (s, 12H), 1.46 (s, 9H). ^{13}C NMR (CD_2Cl_2) δ 189.01, 156.29, 156.19, 150.59, 148.78, 141.84, 140.87, 138.23, 136.15, 134.96, 134.95, 133.43, 133.21, 131.45, 126.87, 126.52, 126.22, 125.32, 121.60, 121.42, 121.03, 120.94, 119.74, 111.06, 110.02, 43.13, 34.73, 33.26, 31.20, 21.84, 21.49. ^{11}B NMR (CD_2Cl_2): δ 45.8. Anal. calcd (%) for $C_{49}H_{44}BNO$: C 87.36, H 6.58, N 2.08; found: C 87.62, H 6.89, N 2.17.

2-(9-Ethyl-9*H*-carbazol-3-yl)-4,4,12,12-tetramethyl-4,12-dihydro-8*H*-3a2-boradibenzo[cd,mn]pyren-8-one (EtCzMeBCO, 3d)

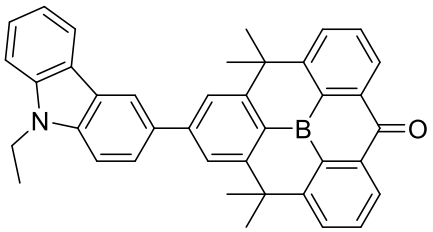

3-Bromo-9-ethyl-2,7-dimethyl-9*H*-carbazole (295 mg, 0.976 mmol) was treated with *n*-BuLi (0.41 mL, 1.01 mmol) in THF (20 mL) at -78 °C. After stirring for 1 h, $B(OMe)_3$ (0.36 mL, 2.93 mmol) was added to the reaction mixture and further stirred for 1 h. The reaction mixture was acidified with 1.0 M HCl (50 mL) at 298 K. The crude product was separated and washed with n-hexane. The resulting (9-ethyl-2,7-dimethyl-9*H*-carbazol-3-yl)boronic acid (220 mg, 0.824 mmol), was combined with Br-BCO (320 mg, 0.749 mmol) in the presence of $Pd(PPh_3)_4$ (48 mg, 0.042 mmol) and K_2CO_3 (158 mg, 1.14 mmol) in THF/H_2O (3:1, v/v, 10 mL). The mixture was refluxed at 90 °C overnight. After cooling down to room temperature, the reaction mixture was filtered using celite pad and washed with dichloromethane. The filtrate was concentrated under reduced pressure and purified by column chromatography on silica gel using dichloromethane/*n*-hexane (1:3, v/v) as eluent to afford **EtCzMeBCO** as a bright yellow solid (Yield: 219 mg, 50%). ^{1}H NMR (CD_2Cl_2) δ 8.26 (d, J = 7.6 Hz, 2H), 8.03 (d, J = 8.0 Hz, 3H), 7.96 (d, J = 7.9 Hz, 1H), 7.88–7.78 (m, 4H), 7.40 (s, 1H), 7.27 (s, 1H), 7.06 (d, J = 7.9 Hz, 1H), 4.39 (q, J = 7.2 Hz, 2H), 2.58 (s, 6H), 1.86 (s, 12H), 1.47 (t, J = 7.2 Hz, 3H). ^{13}C NMR (CD_2Cl_2) δ 189.02, 156.22, 156.18, 148.94, 140.79, 139.85, 138.20, 135.81, 133.90, 133.41, 132.84, 131.47, 126.28, 125.31, 121.23, 121.15, 120.57, 120.40, 119.83, 109.91, 108.89, 43.11, 37.54, 33.24, 21.98, 21.66, 13.62.^{11}B NMR (CD_2Cl_2): δ 47.1. HRMS (EI): *m/z* $[M]^+$ calcd for $C_{41}H_{36}BNO$: 569.2890; found: aaa.aaa. Anal. calcd (%) for $C_{41}H_{36}BNO$: C 86.46, H 6.37, N 2.46; found: C aa.aa, H bb.bb, N cc.cc.

X-ray crystallography

A specimen of suitable size and quality was coated with Paratone oil and mounted onto a glass capillary. The crystallographic measurement was performed using a Bruker Apex II-CCD area detector diffractometer, with graphite-monochromated MoKα radiation (λ = 0.71073 Å). The structure was solved by direct methods, and all nonhydrogen atoms were subjected to anisotropic refinement by full-matrix least-squares on F^2 by using the SHELXTL/PC package. Hydrogen atoms were placed at their geometrically calculated positions and were refined riding on the corresponding carbon atoms with isotropic thermal parameters.

3. Photophysical measurements.

UV-Vis absorption and PL spectra were recorded on a Varian Cary 100, a HORIBA FluoroMax-4P spectrophotometer and a FS5 spectrophotometer, respectively. Solution PL spectra were obtained from oxygen-free and air-saturated toluene solutions (typically 50 μM in toluene). Absolute photoluminescence quantum yields (PLQYs, Φ_{PL}) of solutions were measured on an absolute PL quantum yield spectrophotometer (Quantaurus-QY C11347-11, Hamamatsu Photonics) equipped with a 3.3 inch integrating sphere. Transient PL decays were measured on an FS5 spectrophotometer (Edinburgh Instruments) in either time-correlated single-photon counting (TCSPC) mode (an EPL-375 ps pulsed diode laser as a light source) or multi-channel scaling (MCS) mode (a microsecond Xenon flashlamp as a light source). The lifetimes of prompt fluorescence (τ_p) were estimated by fitting decay curves measured via the TCSPC mode, while those of delayed fluorescence (τ_d) were estimated with curves measured via the MCS mode. The temperature-dependence of PL decay was obtained with an OptistatDN^{TM} cryostat (Oxford Instruments).

4. Cyclic voltammetry

Cyclic voltammetry measurements were carried out in CH_2Cl_2 (1×10^{-3} M) with a three-electrode cell configuration consisting of platinum working and counter electrodes and a $Ag/AgNO_3$ (0.01 M in CH_3CN) reference electrode at room temperature. Tetra-*n*-butylammonium hexafluorophosphate (0.1 M in CH_2Cl_2) was used as the supporting electrolyte. The redox potentials were recorded at a scan rate of 100 mV/s and are reported with reference to the ferrocene/ferrocenium (Fc/Fc^+) redox couple.

III. Results and discussion

1. Synthesis and characterization.

A series of Planar-donor-appended compounds with different donors (**CzMeBCO, BuCzMeBCO and EtCzMeBCO**) were prepared according to **Scheme 1**. The carbazole group, 3-bromo-2,7-dimethyl-9H-carbazole, was prepared from 2,7-dimethyl-9H-carbazole via bromination. The **CzMeBr** and **BuCzMeBr** were prepared using Ullmann reaction amination. **EtCzMeBr** was prepared using potassium carbonate amination. And **Br-BCO** acceptor was prepared from the reported procedure.[26] The final Planar-donor-appended compounds containing BCO acceptors were obtained via Suzuki reaction between **Br-BCO** accepter and **CzMeB(OH)2** donor which was prepared by borylation of **CzMeBr**. The accepter group was introduced that the boron moiety was prevented from nucleophilic attack to the boron center and strengthen the rigidity of molecule. All final compounds were characterized by multinuclear NMR spectroscopy (**Figure 7-10**) and elemental analysis.

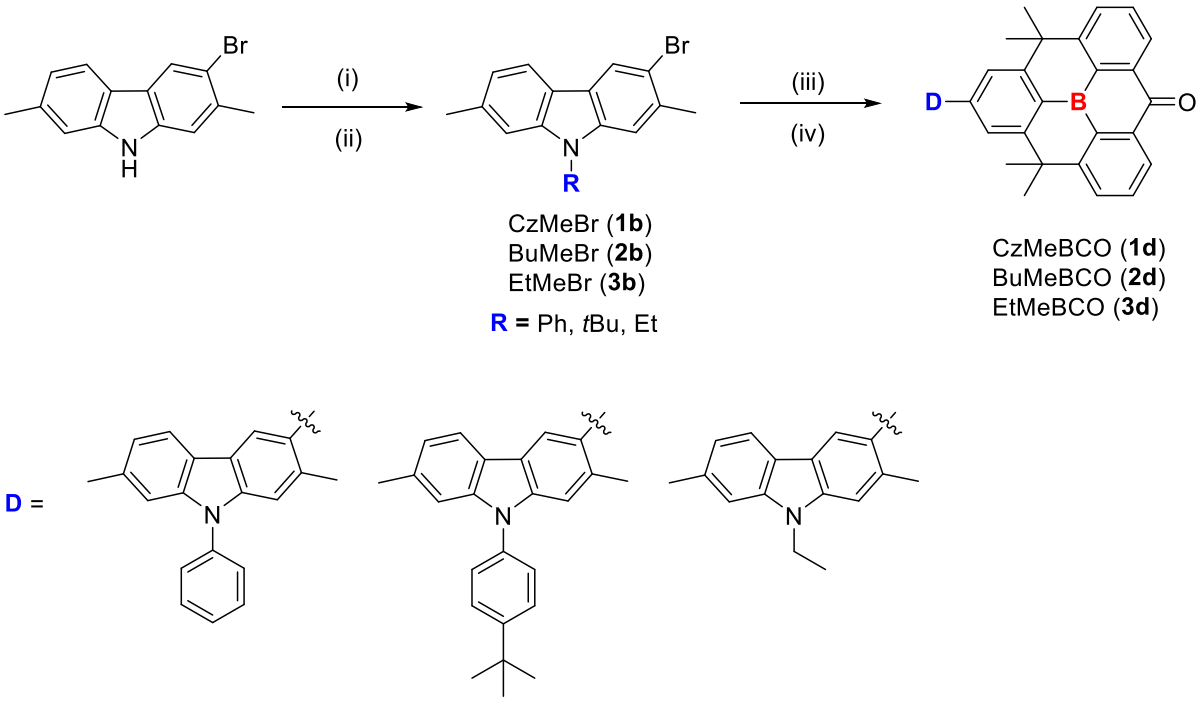

Scheme 1. Condition : (i) Cu, CuI, K_2CO_3, R-I(R = Ph, t-Bop), DMF, reflux, 16 h (**1b, 2b**); (ii) KOH, DMF, RT, 16 h (**3b**); (iii) *n*-BuLi, THF, -78℃, RT, 16 h, then $B(OMe)_3$, HCl; (iv) $Pd(PPh_3)_4$, K_2CO_3, Br-BCO, THF:H2O=3:1, reflux, 16 h (**1d, 2d, 3d**)

The ^{1}H NMR spectra of all compounds exhibits singlet of CH_3 group (δ 1.86 ppm) substituted at the same two dimethyl bridge of BCO and singlet of CH_3 group (δ 2.49 - 2.58

ppm) substituted at the same dimethyl carbazole. The ^{1}H NMR spectra of the **BuCzMeBCO** showed sharp singlet of $(CH_3)_3$ from tert-butyl benzene (δ 1.46 ppm). And **EtCzMeBCO** showed quartet CH_2 and triplet CH_3 from carbazole group (δ 4.39 ppm, 1.47 ppm). As for ^{11}B NMR, a tri-coordinated boron center was detected as a broad singlet at δ 47.06 - 47.8 ppm for all compound**,** which is consistent with the presence of trigonal planar boron center from BCO group. Furthermore, from TGA analysis shows thermal stability, giving T_{d5} value of 387 ºC, 405 ºC, 262 ºC for **CzMeBCO**, **BuCzMeBCO** and **EtCzMeBCO** respectively.

a)

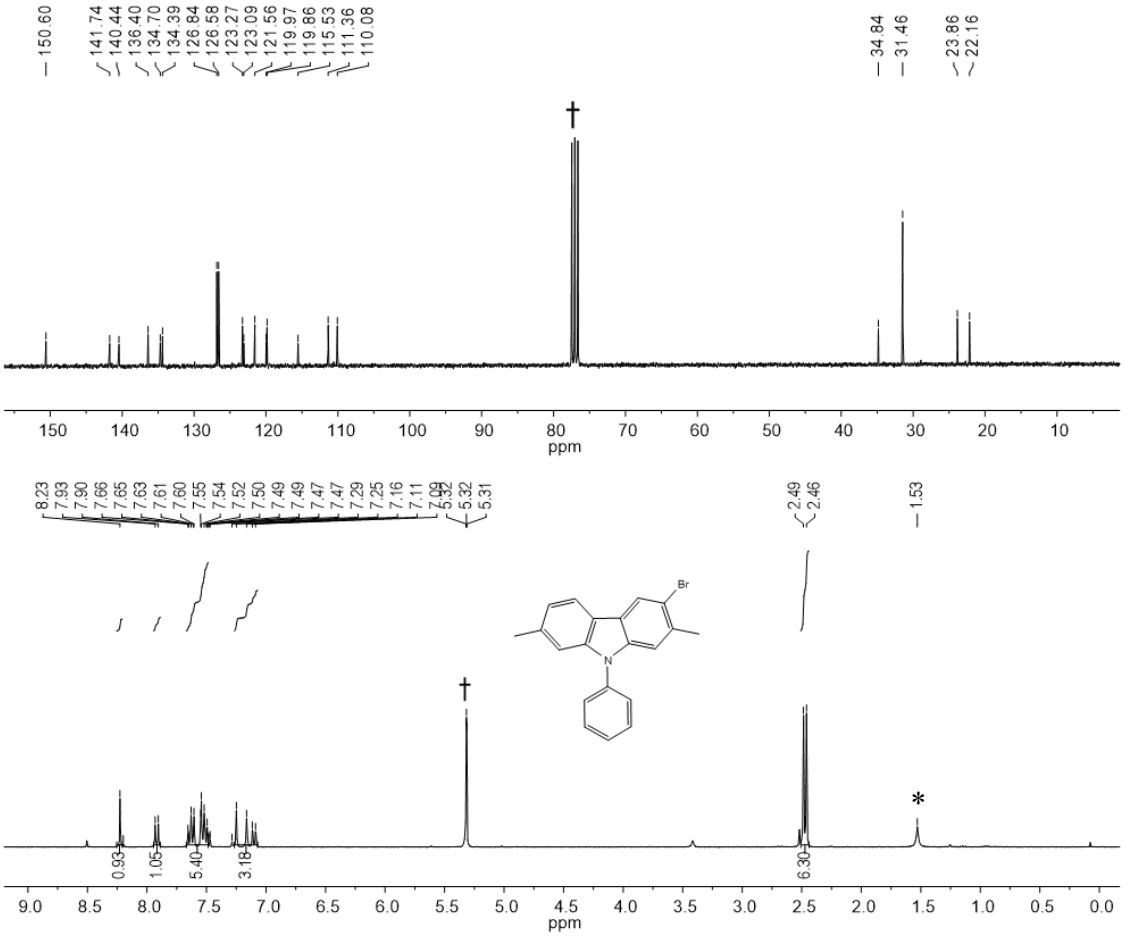

b)

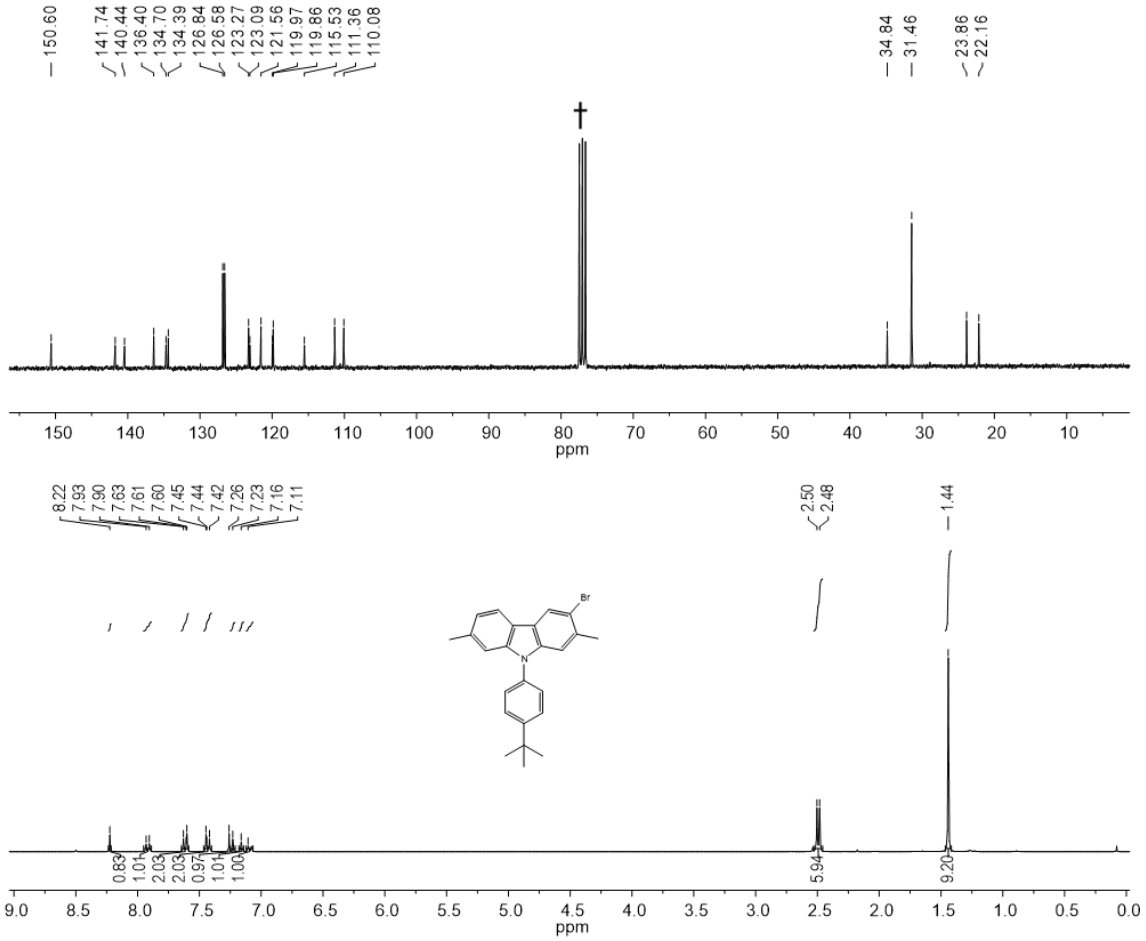
150.60
141.74
140.44
136.40
134.70
134.39
126.84
126.58
123.27
123.09
121.56
119.97
119.86
115.53
111.36
110.08
34.84
31.46
23.86
22.16
†
ppm
8.22
7.93
7.90
7.63
7.61
7.60
7.45
7.44
7.42
7.26
7.23
7.16
7.11
2.50
2.48
1.44
Br
N
0.83
1.01
2.03
2.03
0.97
1.01
1.00
5.94
9.20
ppm

c)

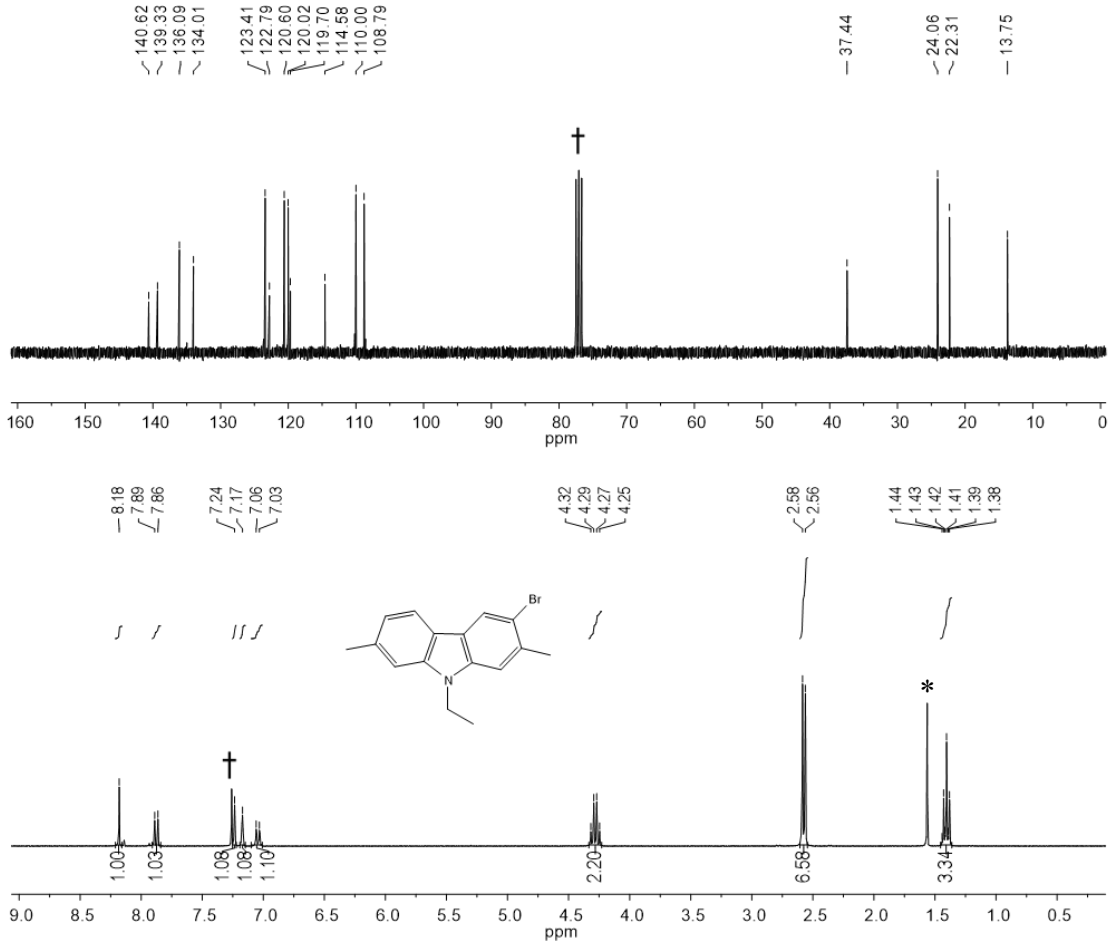

Figure 7. ^{1}H (bottom) and ^{13}C (top) NMR spectra of **CzMeBr** (a) in CD_2Cl_2, **BuCzMeBr** (b) and **EtCzMeBr** (c) in $CDCl_3$. (* from residual H_2O, † from CH_2Cl_2).

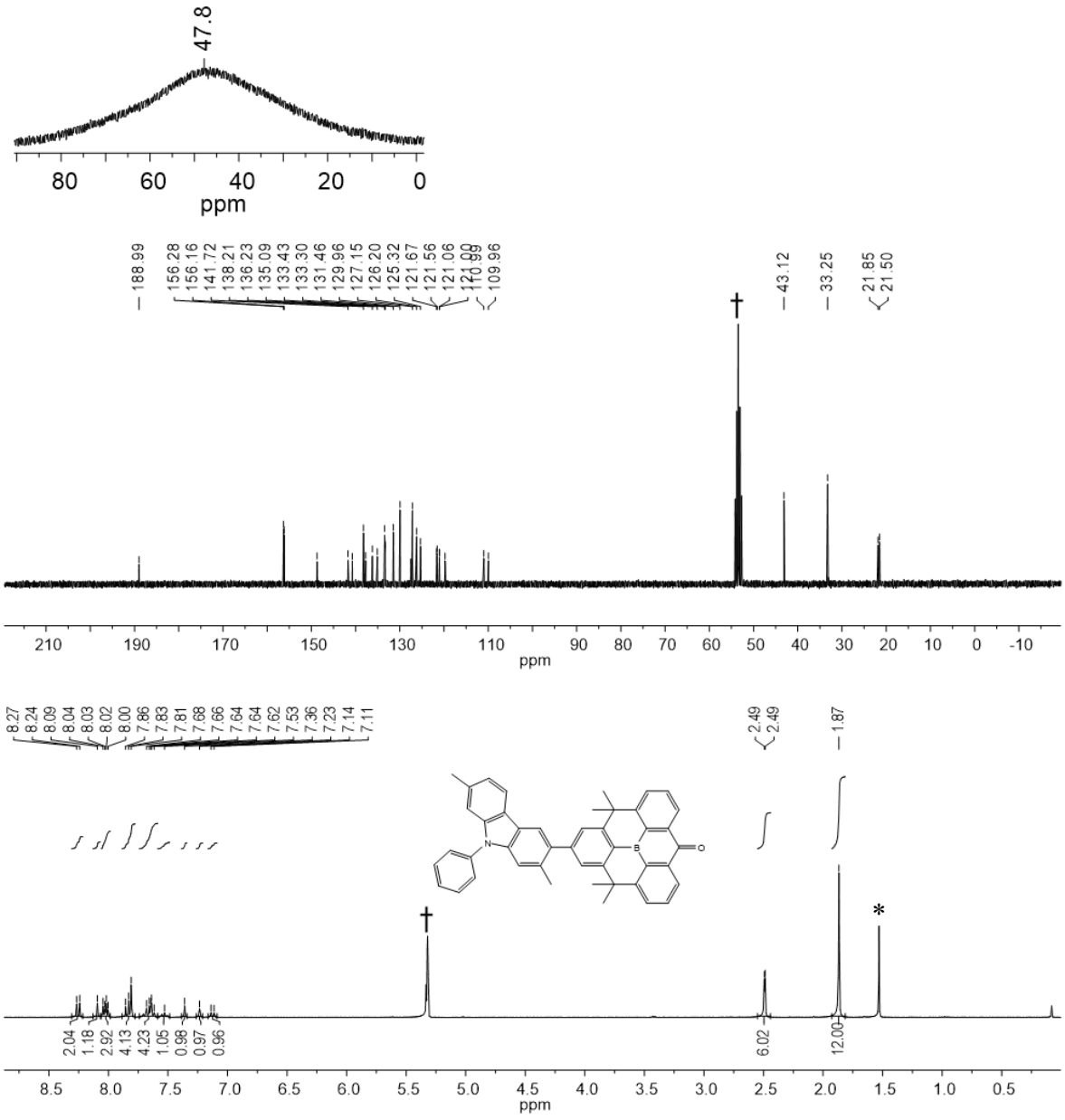

Figure 8. ^{1}H (bottom), ^{13}C (middle), and ^{11}B (top) NMR spectra of **CzMeBCO** in CD_2Cl_2 (* from residual H_2O, † from CH_2Cl_2).

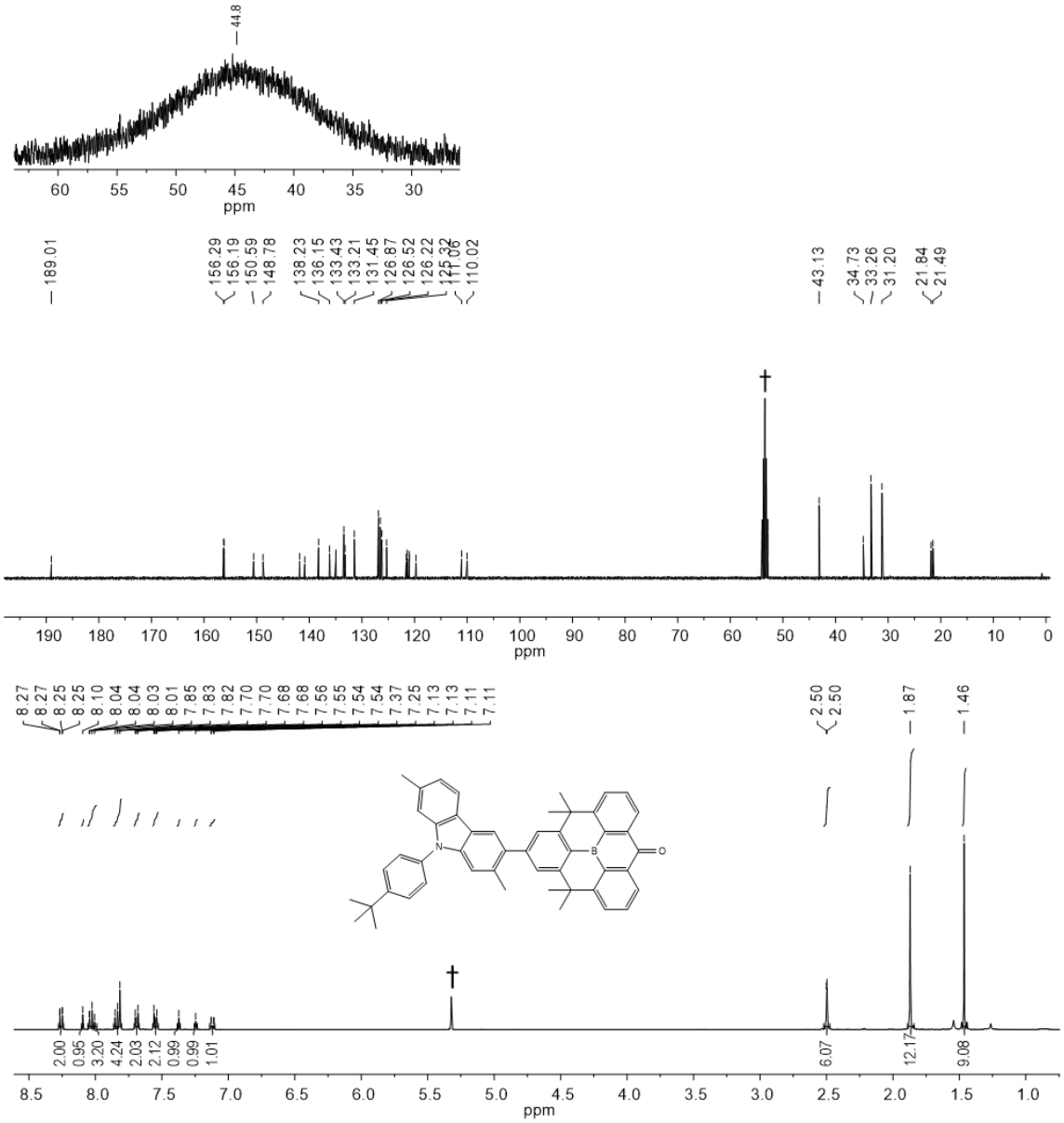

Figure 9. ^{1}H (bottom) and ^{13}C (middle), and ^{11}B (top) NMR spectra of **BuCzMeBCO** in CD_2Cl_2 (* from residual H_2O, † from CH_2Cl_2).

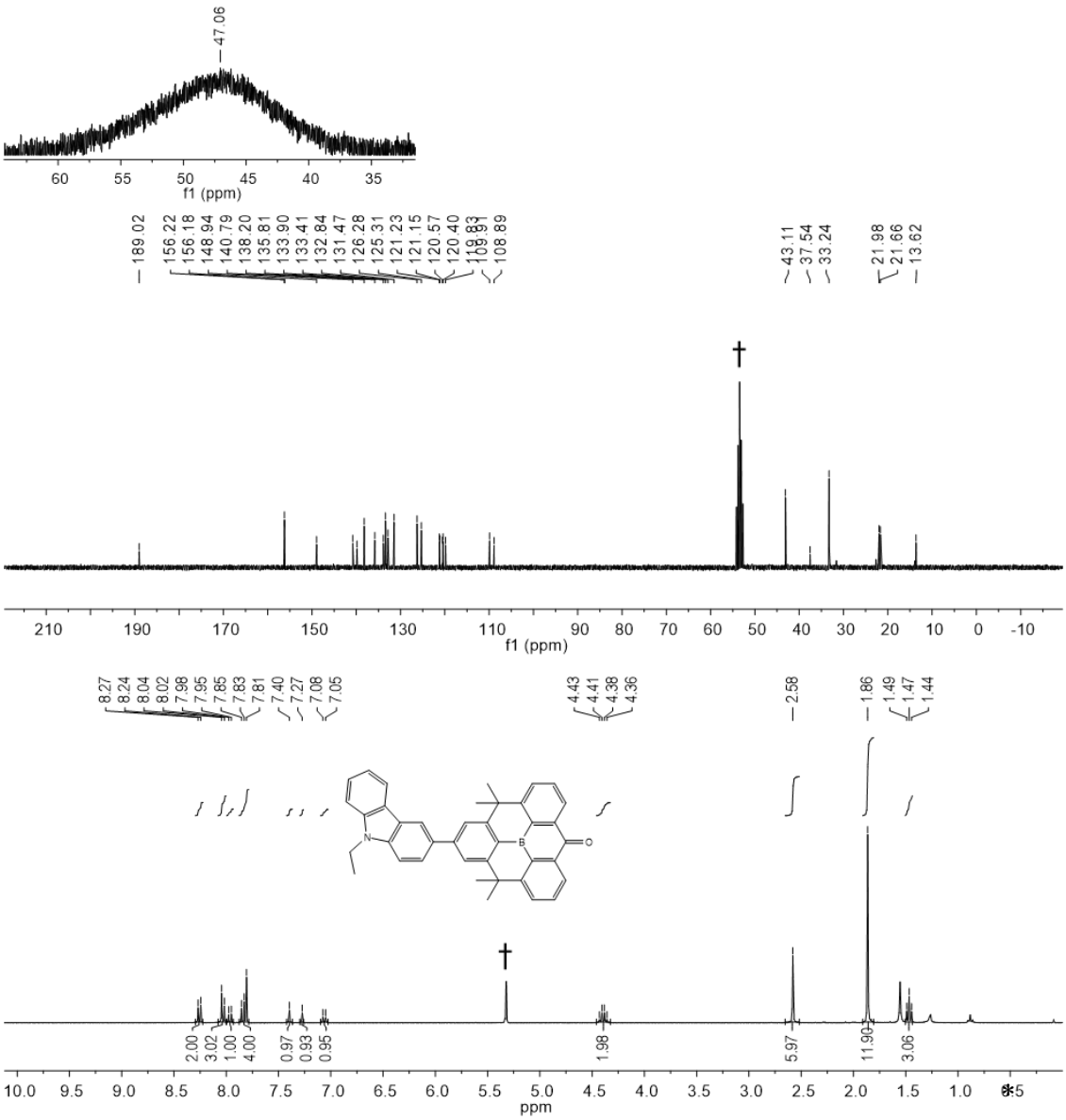

Figure 10. ^{1}H (bottom), ^{13}C (middle) and ^{11}B (top) NMR spectra of **EtCzMeBCO** in CD_2Cl_2 (* from residual H_2O, † from CH_2Cl_2).

2. Crystal structure of BuCzMeBCO (2d).

X-ray diffraction studies on **BuCzMeBCO** distinctly showed nature planar structure in the planar D–A compounds. To make twist, the BuCz has two methyl to get a steric hindrance, as judged by the dihedral angles of 49.24 respectively (**BuCzMeBCO**). The detailed crystallographic data and the selected bond lengths and angles are given in Table. X-ray crystal structures are shown in (**Figure 11**).

Table 1. Selected bond lengths (Å) and angles (°) of **BuCzMeBCO**

	BuCzMeBCO
Lengths(Å)	
B(1)-C(28)	1.505(3)
B(1)-C(33)	1.522(3)
B(1)-C(39)	1.523(3)
O(1)-C(45)	1.218(3)
N(1)-C(15)	1.427(3)
C(9)-C(25)	1.491(3)
Angles (°)	
C(28)-B(1)-C(33)	120.00(17)
C(28)-B(1)-C(39)	119.75(18)
C(33)-B(1)-C(39)	120.24(19)

Table 2. Crystallographic data and parameters for **BuCzMeBCO.**

	BuCzMeBCO
formula	C51 H48 B Cl2 N O
formula weight	772.61
crystal system	Triclinic
space group	P-1
a (Å)	10.2270(4)
b (Å)	10.7569(4)
c (Å)	20.1045(8)
α (°)	86.848
β (°)	82.330
γ (°)	67.6810
V (Å^3)	2027.69(14)
Z	2
ρ_{calc} (g cm^{-3})	1.265
μ (mm^{-1})	0.200
F(000)	816
T (K)	173
hkl range	–12 → 13, –14 → 14, –26 → 26
measd reflns	57641
unique reflns [R_{int}]	10125 (0.0380)
reflns used for refinement	6921
refined parameters	523
R1[a] (I > 2σ(I))	0.0667

wR2[b] all data	0.1823
GOF on F^2	1.047
ρ_{fin} (max/min) (e Å^{-3})	1.011/-0.581

[a] R1 = $\sum||Fo| - |Fc||/\sum|Fo|$. [b] wR2 = $\{[\sum w(Fo^2 - Fc^2)^2]/[\sum w(Fo^2)^2]\}^{1/2}$.

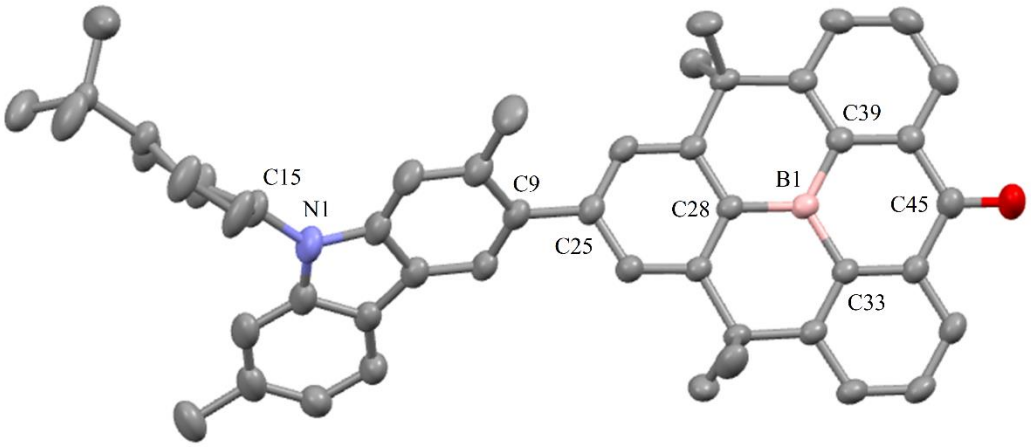

Figure 11. X-ray crystal structures of **BuCzMeBCO** (30% thermal ellipsoids) with atom label. H atoms are omitted for clarity. Color code: blue = nitrogen; brown = boron; red = oxygen.

3. Photophysical Properties

The photophysical properties of all compounds, including UV/Vis absorption and photoluminescence (PL) spectra, were measured in degassed toluene (5.0×10^{-5} M) at 298 K. (**Figure 12** and **Table 3**). All the prepared compounds displayed strong absorption in the high energy region of 250–375 nm that absorption bands from CzMe, BuCzMe, EtCzMe-centered π–π* transition and the triarylboron-centered π–p_π(B) charge transfer (CT) transition.[23] The broad low-energy absorptions (ca. 370–440 nm) can be resulted from intramolecular charge transfer (ICT) transition between the donor and triarylboron acceptors. All compounds show

the PL spectra which is deep blue color emission (**CzMeBCO** = 425 nm; **BuCzMeBCO** = 426 nm; **EtCzMeBCO** = 429 nm). As for PLQY, compound containing tert-butyl carbazole donor exhibited high PLQY (**BuCzMeBCO** = 0.97;) in oxygen free toluene. All compounds have the large decrease of the PLQY in air-saturated toluene that indicates quenching of the T_1 state by triplet oxygen, which in turn implies an efficient $T_1 \rightarrow S_1$ reverse intersystem crossing (RISC) in oxygen-free toluene (**Table 3**). The transient PL decay curves of **1d**, **2d** and **3d** showed one decay components, i.e., just only nanosecond-range prompt (τ_p) component at 298 K (**Figure 14**).

Table 3. Photophysical data of **CzMeBCO**, **BuCzMeBCO**, **EtCzMeBCO**

Compd **D-BAO** **D =**	λ_{abs}[a] [nm]	λ_{PL} [nm]		Φ_{PL} (%)		τ_p /ns(%) [c]		τ_D/μs(%) [d]
		Toluene [a]	Film	Toluene [b] (N_2/air)	PMMA (5 wt%)	Toluene	PMMA (5 wt%)	PMMA (5 wt%)
CzMe	302,342, 347,400	425	493	0.7 (0.01)	0.78	2.45 (99)	10.88 (9)	17.33(91)
BuCzMe	304,343, 396	426	497	0.93(0.03)	0.85	2.47 (100)	9.91 (24)	14.32 (76)
EtCzMe	305, 345, 396	429	513	0.77(0.06)	0.60	3.40 (100)	13.77(65)	1.65 (35)

[a)] In oxygen-free toluene at 298 K (5.0×10^{-5} M); [b)] Absolute photoluminescence quantum yields (PLQYs) in oxygen-free (N_2) and air-saturated (air) toluene at 298 K; [c)] PL lifetimes of prompt (τ_p) decay components for the air-saturated toluene solutions at 298 K. The estimated prompt (Φ_{PF}) portions (%) in transient decay curves are given in parentheses. [d)] PL lifetimes of delayed (τ_d) decay components (oxygen-free toluene solutions and film at 298 K). The estimated delayed (Φ_{DF}) portions (%) in transient decay curves are given in parentheses.

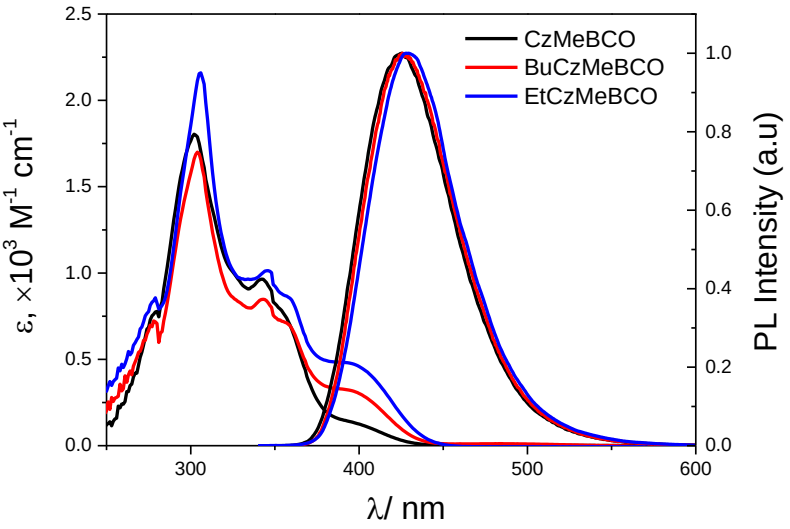

Figure 12. UV/vis absorption (left) and PL spectra (right) of **CzMeBCO, BuCzMeBCO and EtCzMeBCO** in toluene (5.0×10^{-5} M) at 298 K.

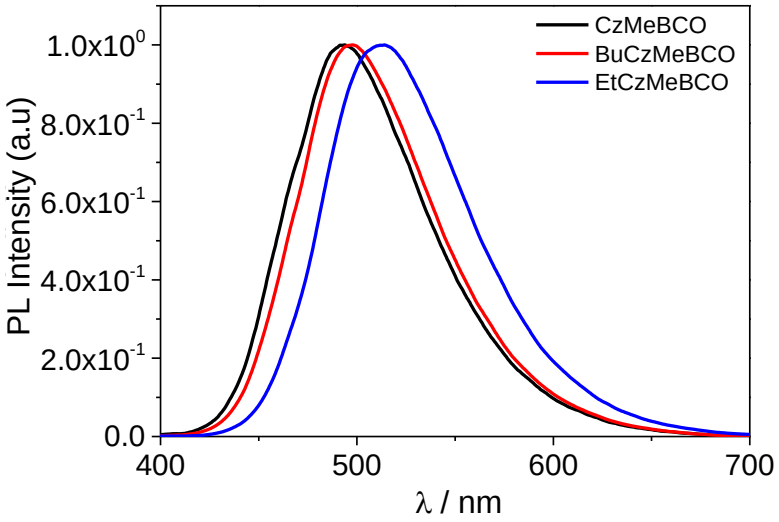

Figure 13. PL spectra of **CzMeBCO, BuCzMeBCO and EtCzMeBCO** in PMMA (5 wt%) at 298 K.

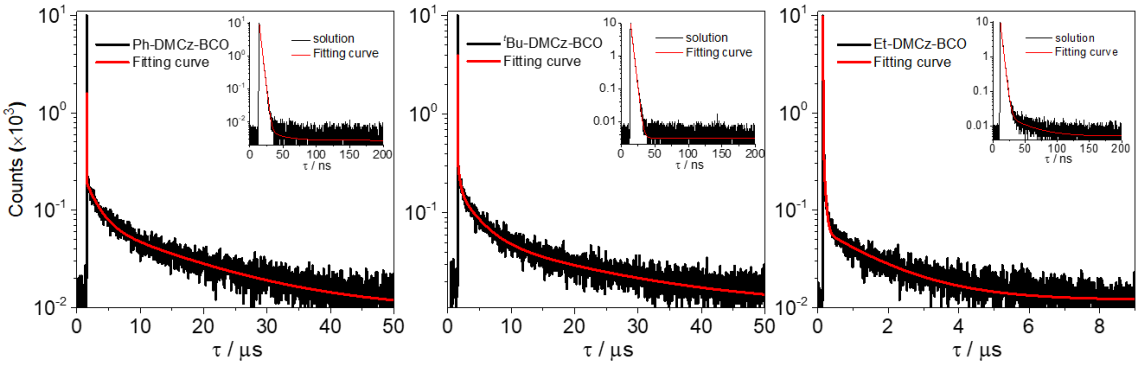

Figure 14. Transient PL decay curves of **CzMeBCO** (left), **BuCzMeBCO** (middle), **EtCzMeBCO** (right) in PMMA (5 wt%) at 298 K. The inset shows the decay curves in oxygen-free (N_2) toluene.

Photophysical properties were also measured in spin-coated PMMA film doped with 5% weight (5 wt%) of compounds (**Figure 14**). Contrary to solution, the photophysical properties of CzMeBCO, BuCzMeBCO, and EtCzMeBCO doped on the host film exhibit moderate TADF with PLQY in a value of 0.60-0.85. This is because that all compounds in the aggregated state can make the dihedral angle (θ) with twisting between donor and acceptor, intramolecular movement is largely inhibited by spatial disturbances and IC channels are blocked. therefore the conjugation was restricted and that leading to an intramolecular charge transfer (ICT) state with a small ΔEst gap.[25] However, in the solution case, these structures are flexible and can not make the dihedral angle (θ). So these exhibit the non-fluorescence by ICT state which is come from D-A conjugation. All compounds in film (i.e. **CzMeBCO** = 493 nm; **BuCzMeBCO** = 497 nm; **EtCzMeBCO** = 513 nm) were red-shifted of ca. 68-84 nm compared to solution data (i.e. **CzMeBCO** = 425 nm; **BuCzMeBCO** = 426 nm; **EtCzMeBCO** = 429 nm). This is because that all compounds have a rigidochromic redshifts.[26]

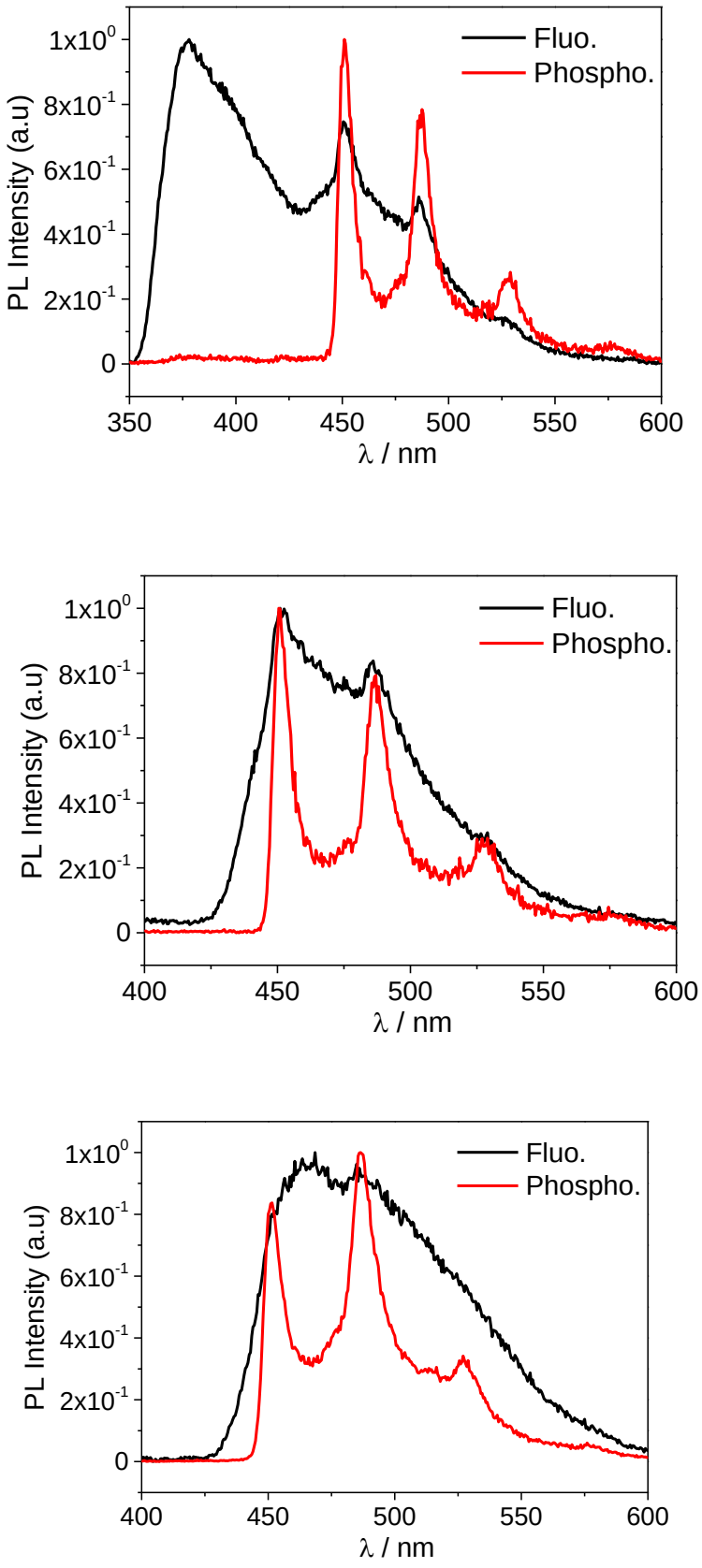

Figure 15. Fluorescence and phosphorescence spectra of **CzMeBCO** (top), **BuCzMeBCO** (middle) and **EtCzMeBCO** (bottom) in toluene at 77 K.

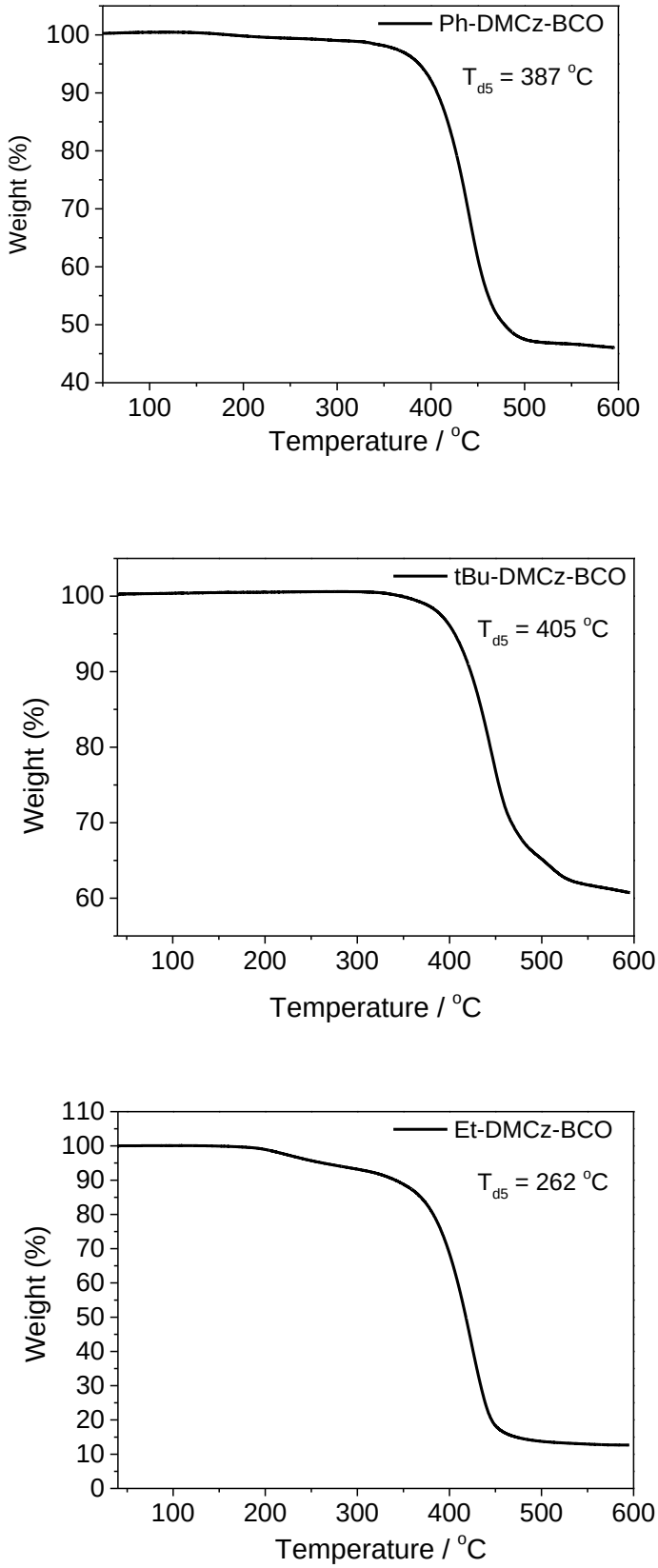

Figure 16. T_{d5} in TGA of **CzMeBCO** (top), **BuCzMeBCO** (middle) and **EtCzMeBCO** (bottom)

Table 4. Photophysical data of **CzMeBCO**, **BuCzMeBCO** and **EtCzMeBCO** at 77 K.

Compound	λ_{PL} [nm]	E_S/E_T[a] [eV]	ΔE_{ST}[b] [meV]
CzMeBCO	451	3.038/3.034	3.7
BuCzMeBCO	450	2.784/2.773	11
EtCzMeBCO	486	2.722/2.716	5.4

[a] E_S and E_T were calculated from the onset of fluorescence and phosphorescence spectra respectively.

[b] $\Delta E_{ST} = E_S - E_T$.

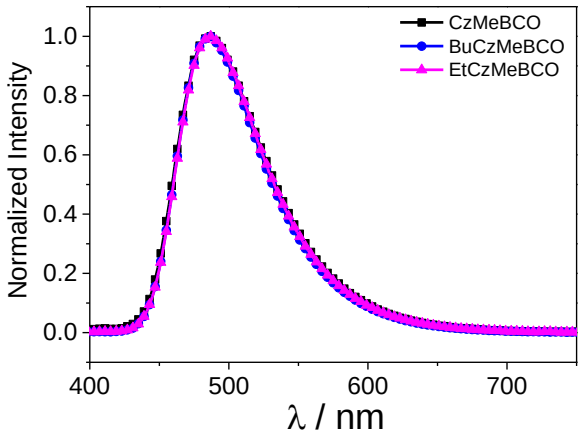

Figure 17. PL spectra of the host films doped with **CzMeBCO** (5 wt%), **BuCzMeBCO** (5 wt%), **EtCzMeBCO(5 wt%)**.

4. Electrochemical Properties

The electrochemistry properties of **CzMeBCO**, **BuCzMeBCO, EtCzMeBCO** were carried out by cyclic voltammetry to understand the character of the frontier orbitals **(Figure 18** and **Table 5**). The half-wave oxidation potentials (E_{ox} versus Fc/Fc^{+}) were 0.722 V (**CzMeBCO**), 0.717 V (**BuCzMeBCO**), 0.625 V (**EtCzMeBCO**) correspond to the irreversible oxidation from donor moieties. **CzMeBCO** and **BuCzMeBCO** showed similar oxidation potential due to the same moieties of dimethylcarbazol with phenyl group but in **EtCzMeBCO** case, that is large than **CzMeBCO** and **BuCzMeBCO** due to donating group.[27] Consequently, their HOMO energy levels determined from the half-wave oxidation potentials were −5.522 eV, −5.517 eV, −5.425 eV respectively. All reduction potentials were estimated from the optical band gap (Eg) and the HOMO levels, giving their calculated LUMO energy levels were −2.656 eV (**CzMeBCO**), −2.667 eV (**BuCzMeBCO**), −2.607 eV (**EtCzMeBCO**) respectively.

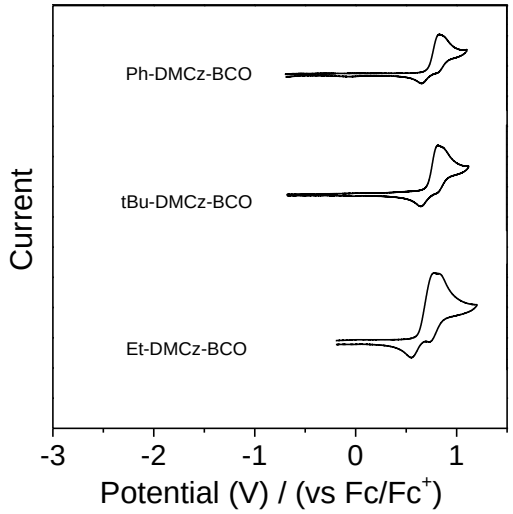

Figure 18. Cyclic voltammograms of **1d**–**3d** (0.5×10^{-3} M in DCM, scan rate = 100 mV/s).

Table 5. Cyclic Voltammetry Data of **CzMeBCO**, **BuCzMeBCO and EtCzMeBCO.**

Compound	E_{ox} [V]	[a]HOMO/LUMO [eV]	E_g[b] [eV]
1d	0.72	–5.52/–2.66	2.86
2d	0.72	–5.52/–2.67	2.86
3d	0.63	–5.42/–2.61	2.82

All reversible oxidation measured with reference to a Fc/Fc^+ redox couple at 298 K. [a]HOMO energy levels were estimated by electrochemical oxidation(-4.8-E1/2 ox), whereas LUMO energy levels were calculated by $E_{HOMO} + E_g$. [b]E_g were estimated by onset of absorption.

5. Solvatochromism

All of the emission bands underwent gradual red shifts with increasing polarity of the solvent These emission features are consistent with the ICT transition in nature.

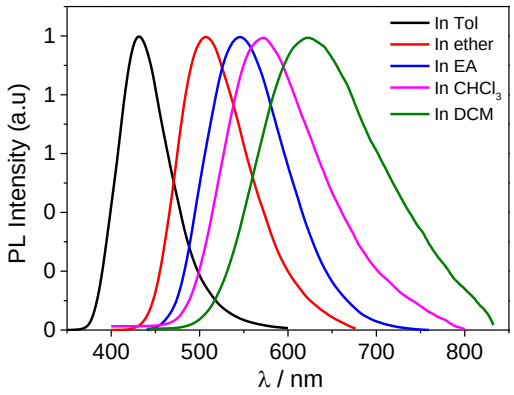

Figure 19. Solvatochromism of **2d** (50 µM in solvents, λ_{ex} = 303 nm).

Table 6. Solvatochromism of **CzMeBCO**, **BuCzMeBCO and EtCzMeBCO.**

Solvent	$\lambda_{PL/nm}$	FWHM (nm)	μ (Debye, D)	ε
Toluene	431	68	0.31	2.38
ether	507	91	1.15	4.33
EA	545	106	1.88	6.02
$CHCl_3$	572	124	1.15	4.81
DCM	622	160	1.14	8.93
Poly(methyl methacrylate), PMMA				3.0

6. Electroluminescent properties

To validate the electroluminescent (EL) properties of the proposed emitters (**1–3d)**, TADF-OLED devices possessing the following structures were fabricated: glass/ ITO (150 nm) / HATCN (5 nm) / NPB (40 nm) / TCTA (10 nm / mCBP:Dopant (30 nm, 5 wt%)/ TmPyPB (40 nm) / LiF (0.7 nm) / Al (90 nm) (**D1**–**D3**). The EL characteristics of the four devices are summarized in **Fig. 20** and **Table 7**. The devices emit skyblue (**D1–D3**) lights, which correspond to the following CIE (x, y) color coordinates: (0.18, 0.38), (0.19, 0.37) and (0.19, 0.38) respectively. The devices incorporating the emitters containing the same acceptor exhibit smilar CIE coordinates. **D1** and **D2** have similar EQEs and the current efficiencies while **D3** is lower than both **D1** and **D2**. Particularly, **D1** and **D2** show maximum EQEs of 14.7% and 14.5%, respectively. Nevertheless, **D1 – D3** underwent efficiency roll-offs at around 1,000 cd m^{-2} due to the increased exciton quenching processes such as triplet-triplet annihilation (TTA) and singlet-triplet annihilation (STA). For **D3**, the maximum EQEs were estimated to be only half of those of **D1** and **D2**.

The efficiencies were much lower than those of the previous devices employing the donor(TMCz, DMAC) - BCO emitters (ca. 24%–28%) [28]. These low device efficiencies could be primarily attributed to the lower PLQYs of the doped host films and expetially dihedral angle of donor(X-CzMe)-BCO was lower than donor(TMCz, DMAC) – BCO. Furthermore, severe efficiency roll-offs were

observed for **D3** as the luminance increased. This indicates that thermal stability of **D3** was much lower than **D1 – D2** might undergo an dicomposing process in low temperature.

Table 7. Device performances of TADF-OLEDs fabricated with **1–3**.

Device[a] (emitter)	λ_{EL} (nm)	CIE (x, y)[b]	V_{on} (V)[c]	EQE (%)[d]	PE (lm W^{-1})[e]	CE (cd A^{-1})[f]
D1 (**1**)	487	(0.19, 0.38)	3.6	14.7 / 11.5	30.2 / 18.6	33.7 / 26.5
D2 (**2**)	487	(0.19, 0.37)	3.6	14.5 / 11.6	28.9 / 18.6	33.0 / 26.4
D3 (**3**)	487	(0.19, 0.38)	3.6	9.6 / 6.7	19.7 / 10.4	22.0 / 15.2

[a] ITO (150 nm) / HATCN (5 nm) / NPB (40 nm) / TCTA (10 nm / mCBP:Dopant (30 nm, 5 wt%)/ TmPyPB (40 nm) / LiF (0.7 nm) / Al (90 nm)
[b] Color coordinates (CIE 1931) at maximum luminance.
[c] Applied voltage at a luminance of 1 cd m^{-2}.
[d] External quantum efficiency: maximum and value at 100 cd m^{-2}.
[e] Power efficiency: maximum and value at 100 cd m^{-2}.
[f] Current efficiency: maximum and value at 100 cd m^{-2}.

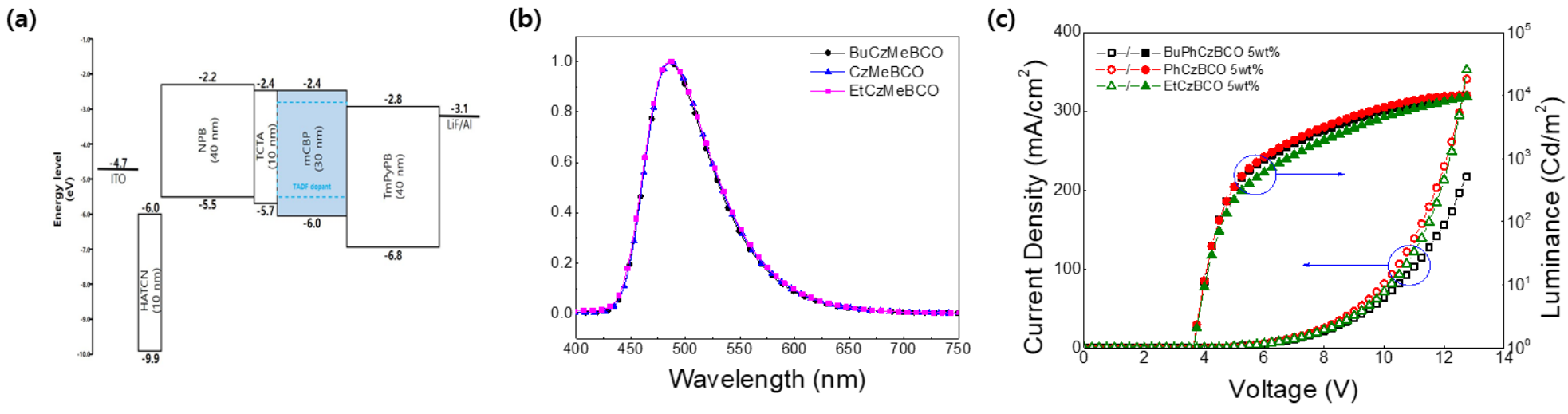

Figure 20. (a) Energy level diagram of the devices (eV) relative to the vacuum level. (b) EL spectra of **D1**–**D3**. (c) Current density-voltage-luminance (*J*–*V*–*L*) characteristics of **D1**–**D3**.

IV. Conclusion

Planar-donor-acceptor containing BCO compounds (**1d**–**3d**) were prepared and characterized through NMR spectroscophy, elemental analysis, X-ray crystallography. All compounds in solution exhibit non-fluorescence which was characterized by UV/Vis, PL, PLQY and lifetime measurements. All compounds show the normal PLQY in the oxygen free toluene. (Φ_{PL} (%) = 79% for **1d**; 93% for **2d;** 77% for **3d**), but lifetime is not appeared. However, All compounds coting on the PMMA film exhibited suitable PLQY (Φ_{PL} (%) = 78% for **1d**; 85% for **2d;** 60% for **3d**) and wavelength which was redshift (68~84 nm) by rigidochromic effect as solid state of compound. All compounds showed normal fluorescence in solution state while they showed TADF (τ_D = 1.65−17.33 μs) in rigid state. BuCzMeBCO has high thermal stability (T_{d5} = 405 ºC) due to C−C bond between donor and acceptor. The findings in this study suggest that the compounds which have C−C bond between donor and acceptor have a good thermal stability. All compounds showed normal fluorescence in solution while TADF−OLEDs employing 1−3 as dopants exhibited sky blue emission, the devices with the CzMe, BuCzMe donor-based emitter displayed device performance with maximum EQEs of over 14% in 5 wt% of dopant. The result from this study gives the prospect as a third generation OLED emitting material containing the newly introduced C−C bond with donor and acceptor.

V. Reference

(1) Negi, S., Mittal, P. & Kumar, B. Impact of different layers on performance of OLED. *Microsyst Technol,* **24,** (2018) 4981–4989. https://doi.org/10.1007/s00542-018-3918-y

(2) Bernanose, A.; Comte, M.; Vouaux, P. "A new method of light emission by certain organic compounds", J. Chim. Phys. **50**: (1953), 64. .

(3) 3 Tang, C. W.; VanSlyke, S. A., Organic electroluminescent diodes, *Applied Physics Letters***,** *51* (1987), (12), 913-915.

(4) Helfrich, W.; Schneider, W. G., Recombination Radiation in Anthracene Crystals, *Physical Review Letters 14,* **(**1965), (7), 229-231.

(5) Lin Ke, Peng; Ramadas, K.; Burden, A.; Soo-Jin, C, "Indium-tin-oxide-free organic light-emitting device". IEEE Transactions on Electron Devices. 53, (2006), (6): 1483–1486. Bibcode:2006ITED...53.1483K. doi:10.1109/TED.2006.874724. S2CID 41905870.

(6) Du, Jian; Chen, Xin-liang; Liu, Cai-chi; Ni, Jian; Hou, Guo-fu; Zhao, Ying; Zhang, Xiao-dan "Highly transparent and conductive indium tin oxide thin films for solar cells grown by reactive thermal evaporation at low temperature",Applied Physics A. **117,** (2014), (2): 815–822. Bibcode:2014ApPhA.tmp..229D. doi:10.1007/s00339-014-8436-x. S2CID 95720073.

(7) Nuyken, O., Jungermann, S., Wiederhirn, V. et al. Modern Trends in Organic Light-Emitting Devices (OLEDs), Monatsh. Chem. 137, (2006), 811–824

(8) N. Thejo Kalyani, S.J. Dhoble / Renewable and Sustainable Energy Reviews 16 (2012) 2696– 2723

(9) Hyein Ha., Young Jae Shim., Min Chul Suh,*: Highly Efficient Solution-Processed Organic Light-Emitting Diodes Containing a New Cross-linkable Hole Transport Material Blended with Commercial Hole Transport Materials, *ACS Appl. Mater. Interfaces* (2021), 21954–21963

(10) Rakhi Grover, Ritu Srivastava, M.N. Kamalasanan, D.S. Mehta,; Novel organic electron injection layer for efficient and stable organic light emitting diodes, Journal of Luminescence, (2014), Volume 146, Pages 53-56, ISSN 0022-2313, https://doi.org/10.1016/j.jlumin.2013.09.004.

(11) Junsheng Yu, Shuangling Lou, Yadong Jiang, Lu Li, Qing Li, and Xiaowei Zhan "Novel hole blocking material for organic light-emitting devices", Proc. SPIE 6722, 3rd International Symposium on Advanced Optical Manufacturing and Testing Technologies, Advanced Optical Manufacturing Technologies, (2007), 67221L https://doi.org/10.1117/12.783010

(12) Chihaya, Adachi.; Atula S. D.; Sandanayaka.; The Leap from Organic Light-Emitting Diodes to Organic Semiconductor Laser Diodes CCS Chem. (2020), 2, 1203–1216

(13) The Authors. Published by WILEY-VCH Verlag GmbH & Co. KGaA, Weinheim Adv. Mater. 29 (2017), 1605444

(14) Kim, J.U., Park, I.S., Chan, CY. et al. Nanosecond-time-scale delayed fluorescence molecule for deep-blue OLEDs with small efficiency rolloff. Nat Commun 11, (2020), 1765 *https://doi.org/10.1038/s41467-020-*

15558-5

(15) Manna, M. K.; Shokri, S.; Wiederrecht, G. P.; Gosztola, D. J.; Ayitou, A. J., New perspectives for triplet-triplet annihilation based photon upconversion using all-organic energy donor & acceptor chromophores. Chem Commun (Camb) 54 (2018), (46), 5809-5818.

(16) S. Hirata, Y. Sakai, K. Masui, H. Tanaka, S.Y. Lee, H. Nomura, N. Nakamura, M. Yasumatsu, H. Nakanotani, Q. Zhang, K. Shizu, H. Miyazaki, C. Adachi, Highly efficient blue electroluminescence based on thermally activated delayed fluorescence, Nat. Mater. 14 (2015), 330–336.

(17) ACS Appl. Mater. Interfaces 2019, 11, 30, 27125–27133 Publication Date:July 17, 2019 *https://doi.org/10.1021/acsami.9b06364*

(18) Acc. Chem. Res. 2018, 51, 9, 2215–2224 https://doi.org/10.1021/acs.accounts.8b00174

(19) ACS Appl. Mater. Interfaces 2019, 11, 30, 27125–27133 *https://doi.org/10.1021/acsami.9b06364*

(20) Z.-B. Sun, et al., Triarylborane p-electron systems with intramolecular charge-transfer transitions, Chin. Chem. Lett. (2016). http://dx.doi.org/10.1016/j.cclet.2016.06.007

(21) P.J. Grisdale, J.L.R. Williams, M.E. Glogowski, B.E. Babb, Boron photochemistry. 448 Possible role of bridged intermediates in the photolysis of borate complexes, J. 449 Org. Chem. 544–549 (1971), 450 S. Hirata, Y. Sakai, K. Masui, H. Tanaka, S.Y. Lee, H. Nomura, N. Nakamura, M. Yasumatsu, H. Nakanotani, Q. Zhang, K. Shizu, H. Miyazaki, C. Adachi, Highly efficient blue electroluminescence based on thermally activated delayed fluorescence, Nat. Mater. 14 (2015) 330–336.

(22) W. Kaim, A. Schulz, p-Phenylenediboranes: mirror images of p-phenylene- 454 diamines, Angew. Chem. Int. Ed. 23 (1984), 615–616; 455

(23) Z.G. Zhou, A. Wakamiya, T. Kushida, S. Yamaguchi, Planarized triarylboranes: 627 stabilization by structural constraint and their plane-to-bowl conversion, J. Am. 628 Chem. Soc. 134 (2012), 4529–4532;

(24) Wong, M. Y.; Zysman-Colman, E., Purely Organic Thermally Activated Delayed Fluorescence Materials for Organic Light-Emitting Diodes. *Adv Mater 29* (22) (2017),

(25) Cai Z, Chen H, Guo J, Zhao Z and Tang BZ,; Efficient Aggregation-InducedDelayed Fluorescence Luminogens for Solution-Processed OLEDs With Small Efficiency Roll-Off. Front. Chem.8 (2020), 193. doi:10.3389/fchem.2020.00193

(26) Lee, Y. H., Lee, D., Lee, T., Lee, J., Jung, J., Yoo, S., & Lee, M. H. Impact of boryl acceptors in para-acridine-appended triarylboron emitters on blue thermally activated delayed fluorescence OLEDs. Dyes and Pigments, (2021), 188. https://doi.org/10.1016/j.dyepig.2021.109224

(27) Tang, C., Chen, J., Li, Y. et al. Alkyl-Substituted Carbazole/Pyridine Hybrid Host Materials for Efficient Solution-Processable Blue- and Green-Emitting Phosphorescent OLEDs. Electron. Mater. Lett. 2021, 17, 148–156